Gastroenterology 2021;161:1982–1997

BASIC AND TRANSLATIONAL—LIVER

Hepatic miR-144 Drives Fumarase Activity Preventing NRF2 Activation During Obesity

Valerio Azzimato,[1] Ping Chen,[1] Emelie Barreby,[1] Cecilia Morgantini,[1] Laura Levi,[1] Ana Vankova,[1] Jennifer Jager,[2] André Sulen,[1] Marina Diotallevi,[3,4] Joanne X. Shen,[5] Anne Miller,[6] Ewa Ellis,[7] Mikael Rydén,[8] Erik Näslund,[9] Anders Thorell,[9,10] Volker M. Lauschke,[5,11] Keith M. Channon,[3,4] Mark J. Crabtree,[3,4] Arvand Haschemi,[6] Siobhan M. Craige,[12] Mattia Mori,[13] Francesco Spallotta,[14] and Myriam Aouadi[1]

[1]Center for Infectious Medicine (CIM), Department of Medicine, Karolinska Institutet, Huddinge, Sweden; [2]Université Côte d'Azur, Inserm, Centre Méditerranéen de Médecine Moléculaire (C3M), Team «Cellular and Molecular Pathophysiology of Obesity and Diabetes», Côte d'Azur, France; [3]BHF Centre of Research Excellence, Division of Cardiovascular Medicine, Radcliffe Department of Medicine, John Radcliffe Hospital, University of Oxford, Oxford, UK; [4]Wellcome Centre for Human Genetics, University of Oxford, Oxford, UK; [5]Department of Physiology and Pharmacology, Karolinska Institutet, Solna, Sweden; [6]Department of Laboratory Medicine, Medical University of Vienna, Vienna, Austria; [7]Division of Transplantation Surgery, Department of Clinical Science, Intervention and Technology (CLINTEC), Karolinska Institutet, Stockholm, Sweden; [8]Department of Medicine (H7), Karolinska Institutet, Huddinge, Sweden; [9]Department of Clinical Sciences, Danderyd Hospital, Karolinska Institutet, Stockholm, Sweden; [10]Department of Surgery, Ersta Hospital, Stockholm, Sweden; [11]Dr Margarete Fischer-Bosch Institute of Clinical Pharmacology, Stuttgart, Germany; [12]Department of Human Nutrition, Foods, and Exercise, Virginia Tech, Blacksburg, Virginia; [13]Department of Biotechnology, Chemistry and Pharmacy, University of Siena, Siena, Italy; and [14]Institute for Systems Analysis and Computer Science "A. Ruberti," National Research Council (IASI – CNR), Rome, Italy

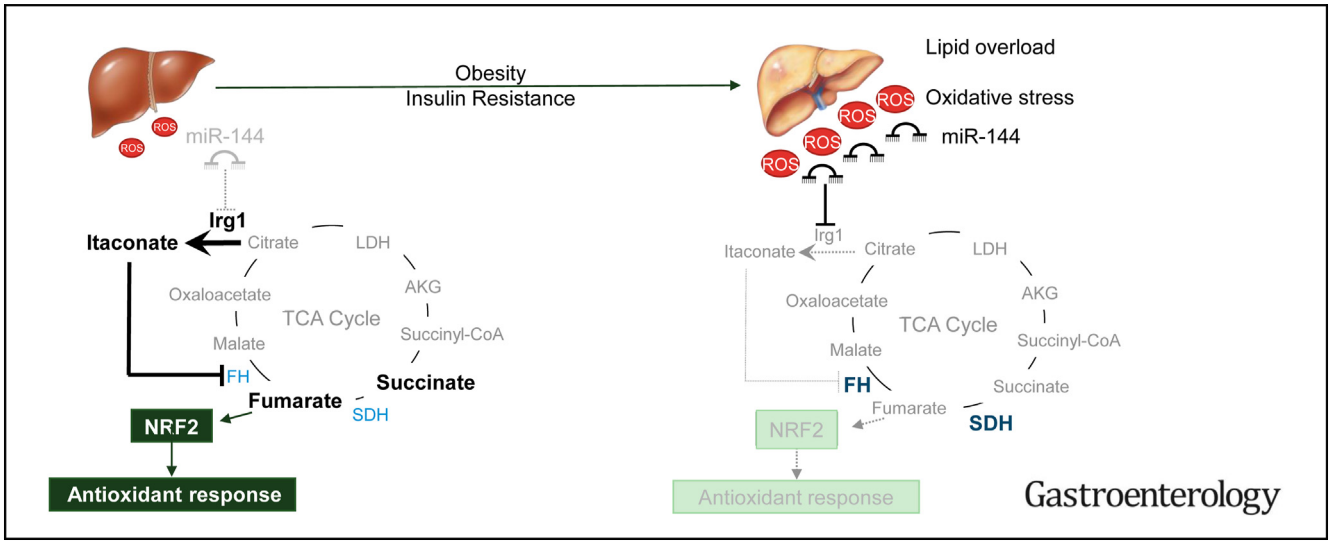

BACKGROUND AND AIMS: Oxidative stress plays a key role in the development of metabolic complications associated with obesity, including insulin resistance and the most common chronic liver disease worldwide, nonalcoholic fatty liver disease. We have recently discovered that the microRNA miR-144 regulates protein levels of the master mediator of the antioxidant response, nuclear factor erythroid 2-related factor 2 (NRF2). On miR-144 silencing, the expression of NRF2 target genes was significantly upregulated, suggesting that miR-144 controls NRF2 at the level of both protein expression *and* activity. Here we explored a mechanism whereby hepatic miR-144 inhibited NRF2 activity upon obesity via the regulation of the tricarboxylic acid (TCA) metabolite, fumarate, a potent activator of NRF2. **METHODS:** We performed transcriptomic analysis in liver macrophages (LMs) of obese mice and identified the immuno-responsive gene 1 (*Irg1*) as a target of miR-144. IRG1 catalyzes the production of a TCA derivative, itaconate, an inhibitor of succinate dehydrogenase (SDH). TCA enzyme activities and kinetics were analyzed after miR-144 silencing in obese mice and human liver organoids using single-cell activity assays in situ and molecular dynamic simulations. **RESULTS:** Increased levels of miR-144 in obesity were associated with reduced expression of *Irg1,* which was restored on miR-144 silencing in vitro and in vivo. Furthermore, miR-144 overexpression reduces *Irg1* expression and the production of itaconate in vitro. In alignment with the reduction in *IRG1* levels and itaconate production, we observed an upregulation of SDH activity during obesity. Surprisingly, however, fumarate hydratase (FH) activity was also upregulated in obese livers, leading to the depletion of its substrate fumarate.

miR-144 silencing selectively reduced the activities of both SDH and FH resulting in the accumulation of their related substrates succinate and fumarate. Moreover, molecular dynamics analyses revealed the potential role of itaconate as a competitive inhibitor of not only SDH but also FH. Combined, these results demonstrate that silencing of miR-144 inhibits the *activity* of NRF2 through decreased fumarate production in obesity. **CONCLUSIONS:** Herein we unravel a novel mechanism whereby miR-144 inhibits NRF2 activity through the consumption of fumarate by activation of FH. Our study demonstrates that hepatic miR-144 triggers a hyperactive FH in the TCA cycle leading to an impaired antioxidant response in obesity.

Keywords: Liver; Metabolism; Oxidative Stress; miRNAs; Fumarase.

WHAT YOU NEED TO KNOW

BACKGROUND AND CONTEXT

Obesity, insulin resistance, and nonalcoholic fatty liver disease are characterized by excessive oxidative stress and dysregulated intracellular metabolism.

NEW FINDINGS

Hepatic miR-144 targets *Irg1*, leading to itaconate reduction and to hyperactivation of fumarase in obese mice and human individuals. Specific silencing of miR-144 rescued itaconate inhibitory effect on fumarase and increased intracellular levels of fumarate, ultimately increasing NFR2 activity in obese mice, human non-parenchymal cells, and in human liver organoids.

LIMITATIONS

Itaconate detection was assessed in the murine RAW 264.7 cell line treated with an miR-144 mimic. In human non-parenchymal cells and liver spheroids, we used *Irg1* as biosensor. Novel methodologies to easily detect itaconate intracellular levels independently of lipopolysaccharide-treated macrophages are required.

IMPACT

Targeting of miR-144 in the liver could represent a novel therapeutic approach in the treatment of metabolic diseases.

Obesity represents a global health issue, as one of the consequences of the worldwide increase in overweight is the increased prevalence of several metabolic complications, including insulin resistance, type 2 diabetes,[1,2] and nonalcoholic fatty liver disease (NAFLD).[3] NAFLD encompasses a spectrum of liver lesions that includes simple steatosis that could eventually lead to the development of nonalcoholic steatohepatitis (NASH), fibrosis, and cirrhosis.[4] NAFLD is accompanied by the excessive production of reactive oxygen species (ROS) and oxidative stress, factors that are considered to be important drivers of NASH, and are thought to promote hepatocyte cell death and the ensuing inflammatory and reparative responses that lead to fibrosis and if unresolved, cirrhosis.[5,6] Obesity and insulin resistance are major risk factors of NAFLD, as approximately 70% of obese patients with type 2 diabetes have NAFLD.[7,8] We recently unraveled a crucial role of liver macrophages (LMs) in the progression of obesity-associated insulin resistance independently of their inflammatory status.[9]

The liver is a central organ responsible for metabolism.[10] Being characterized by a large number and density of mitochondria, liver provides metabolic fuels for itself and the rest of the body.[11] Mitochondria are crucial to hepatic function and a major source of intracellular ROS generation,[12–14] therefore inadequate mitochondrial adaptation is likely a central player in the pathologic progression from obesity to NAFLD and eventually NASH.[8,11,15–17]

MicroRNAs (miRNAs) are short, single-stranded non-coding RNAs of approximately 21 to 23 nucleotides in length[18] that bind to target messenger RNAs (mRNAs) resulting in their degradation and/or inhibiting protein translation.[19] Emerging evidence suggests that miRNAs are able to regulate mitochondrial function at the post-transcriptional level, affecting homeostasis, energy metabolism, oxidative stress, and apoptosis under physiological and pathological conditions.[20,21] Our previous work demonstrated that, in obesity and insulin resistance, LMs express miR-144, an miRNA that targets nuclear factor E2-related factor 2 (NRF2) protein.[22]

Specifically, we showed that LM-specific miR-144 silencing restored the endogenous antioxidant response, increased NRF2 protein levels, activating its downstream targets *NQO1* and *GSTP1*.[22] These results suggested that miR-144 could also regulate the *activity* of NRF2. Phosphorylation serves as a critical posttranslational modification of NRF2 and is involved in multiple aspects of its regulation.[23,24] These posttranslational modifications might affect NRF2 homeostasis, activity, and nuclear export.[24–28] Intracellular metabolites are crucial regulators of NRF2 phosphorylation and activity.[29,30] Specifically, it has been shown that fumarate accumulation resulting from a reduction in fumarate hydratase (FH) activity can directly increase NRF2 phosphorylation.[31–33]

Here, we found that immunoresponsive gene 1 (*Irg1*), a gene involved in cellular metabolism, is a new target of miR-144. *Irg1* produces a tricarboxylic acid (TCA)-derivative, itaconate, which can influence NRF2 function,[34] thus we aimed to investigate whether miR-144 regulates cellular metabolism during obesity, leading to differential NRF2 activity. We demonstrate that, in human obese individuals and mouse models of obesity-induced insulin resistance characterized by excessive hepatic lipid accumulation, miR-

Abbreviations used in this paper: **4-OI, 4-Octyl Itaconate; CUL3, cullin 3; FFA, free fatty acid; FH, fumarate hydratase; GeRPs, glucan-encapsulated RNAi particles; HFD, high-fat diet; IRG1, immunoresponsive gene 1; KEAP1, Kelch-like ECH-associated protein 1; NAFLD, nonalcoholic fatty liver disease; LM, liver macrophages; LPS, lipopolysaccharide; mRNA, messesnger RNA; miRNA, microRNA; NASH, nonalcoholic steatohepatitis; NPCs, non-parenchymal cells; NRF2, nuclear factor erythroid 2-related factor 2; ROS, reactive oxygen species; SDH, succinate dehydrogenase; TCA, tricarboxylic acid; TNF-α, tumor necrosis factor alpha.**

Most current article

0016-5085
https://doi.org/10.1053/j.gastro.2021.08.030

144 is able to impair intracellular liver metabolism and NRF2 activity through regulation of specific enzymes and metabolites of the TCA cycle.

Methods

Human Subjects

Liver samples were obtained from a total of 15 individuals. Key clinical data, homeostatic model assessment for insulin resistance (HOMA-IR) parameters and expression levels of miR-144 and NRF2 protein have been already published in Azzimato et al.[22] Details are provided in the Supplementary Materials.

Cell Cultures and Treatments

Details are provided in the Supplementary Materials.

Mice and Diet

Four-week-old wild-type C57BL/6J (WT) and 5-week-old *ob/ob* male mice were obtained from Charles River Laboratories International, Inc. (Wilmington, MA) and maintained on a 12-hour light/dark cycle. Metabolic parameters such as glucose tolerance test, mice weight, miR-144 expression, and NRF2 protein levels in livers have been published in Azzimato et al.[22] Details are provided in the Supplementary Materials.

Glucan-Encapsulated RNA Interference Particle Administration by Intravenous Injection In Vivo

Glucan-encapsulated RNA interference particles (GeRPs) were prepared as previously described.[35] Details are provided in the Supplementary Materials.

Isolation of LMs and Hepatocytes From Mice

LMs and hepatocytes were isolated as previously described.[36] Details are provided in the Supplementary Materials.

Isolation of LMs From Humans and 4-Octyl Itaconate Treatment

Human liver samples used for isolation of NPCs were collected from patients undergoing liver resection surgery for primary or secondary liver malignancies, in which only non-tumor tissue was used. Details are provided in the Supplementary Materials.

Intracellular Itaconate Measurement

Itaconate levels were measured using high-performance liquid chromatography. Details are provided in the Supplementary Materials.

Metabolic Assays and In Situ Single-Cell Activity Assays

Details are provided in the Supplementary Materials.

Isolation of RNA, miRNA, Real-Time Quantitative PCR and RNA Library Preparation

Total RNA and miRNAs extraction and purification was performed using the TRIzol Reagent or the (Thermo Fisher Scientific) or the miRNeasy mini kit (Qiagen) following the manufacturers' protocol. Details are provided in the Supplementary Materials.

Nuclei and Library Preparation for Global Run-On Sequencing

Details are provided in the Supplementary Materials.

Molecular Dynamics Simulations

The full-length homo-dimeric human FH coded by PDB ID: 3E04 was used as the reference structure in this computational study. Details are provided in the Supplementary Materials.

Liver Spheroids

antagomiR transfections.. Cryopreserved primary human hepatocytes (Heps) (Bioreclamation IVT, Westbury, NY) were mixed with a pre-incubated mixture of Lipofectamine RNAiMAX (Invitrogen, Carlsbad, CA) and amiR/inhibitor constructs (1 nmol amiR/inhibitor per 300,000 cells) in OptiMEM (Gibco, Waltham, MA). Details are provided in the Supplementary Materials.

Western Blot and Immunoprecipitation Assay

An amount of 30 μg of proteins were fractionated by sodium dodecyl sulfate–polyacrylamide gel electrophoresis using precast 4% to 12% gradient gels (ThermoFisher Scientific, Waltham, MA), transferred to polyvinylidene difluoride membranes (ThermoFisher Scientific) and probed with an appropriate dilution of the primary antibodies. Details are provided in the Supplementary Materials.

Bioinformatics

Details are provided in the Supplementary Materials.

Statistical Analysis

Statistical significance of differences among groups was analyzed whenever appropriate with 1-way or 2-way analysis of variance with appropriate post hoc analyses or nonparametric Mann-Whitney *U* tests using GraphPad Prism 8.0 (La Jolla, CA). Data were presented as means ± SEM. *P* values $<.05$ were considered as statistically significant. Sample sizes for each experiment were calculated on the basis of previous data collection and as described in Rosner.[37] Although we started every in vivo experiment with the same number of animals per group, if any individual animal showed any sign of discomfort or if an injection failed, we terminated the study for this particular animal in accordance with our ethical permit.

Results

miR-144 Predicted Target Irg1 Is Downregulated in Obesity-Induced Insulin-Resistant Livers

To investigate the metabolic response of LMs to stress on obesity, we performed an RNA sequencing (RNA-seq)–based gene ontology (GO) enrichment analysis on genes differentially expressed in LMs isolated from a genetic model of obesity (*ob/ob*) compared with controls at 2 different ages (9 and 14 weeks) (Figure 1*A*). These analyses

revealed that multiple pathways involved in metabolic and oxidative stress and energy metabolism were significantly enriched in obese mice compared with controls (see Figure 1*A* and Supplementary Figure 1*A*). Similar results were found in a diet-induced model of obesity, after 9 weeks of high-fat diet (HFD) compared with control littermates fed a normal diet (see Supplementary Figure 1*B*). In addition, GO enrichment analysis of global run-on sequencing, which

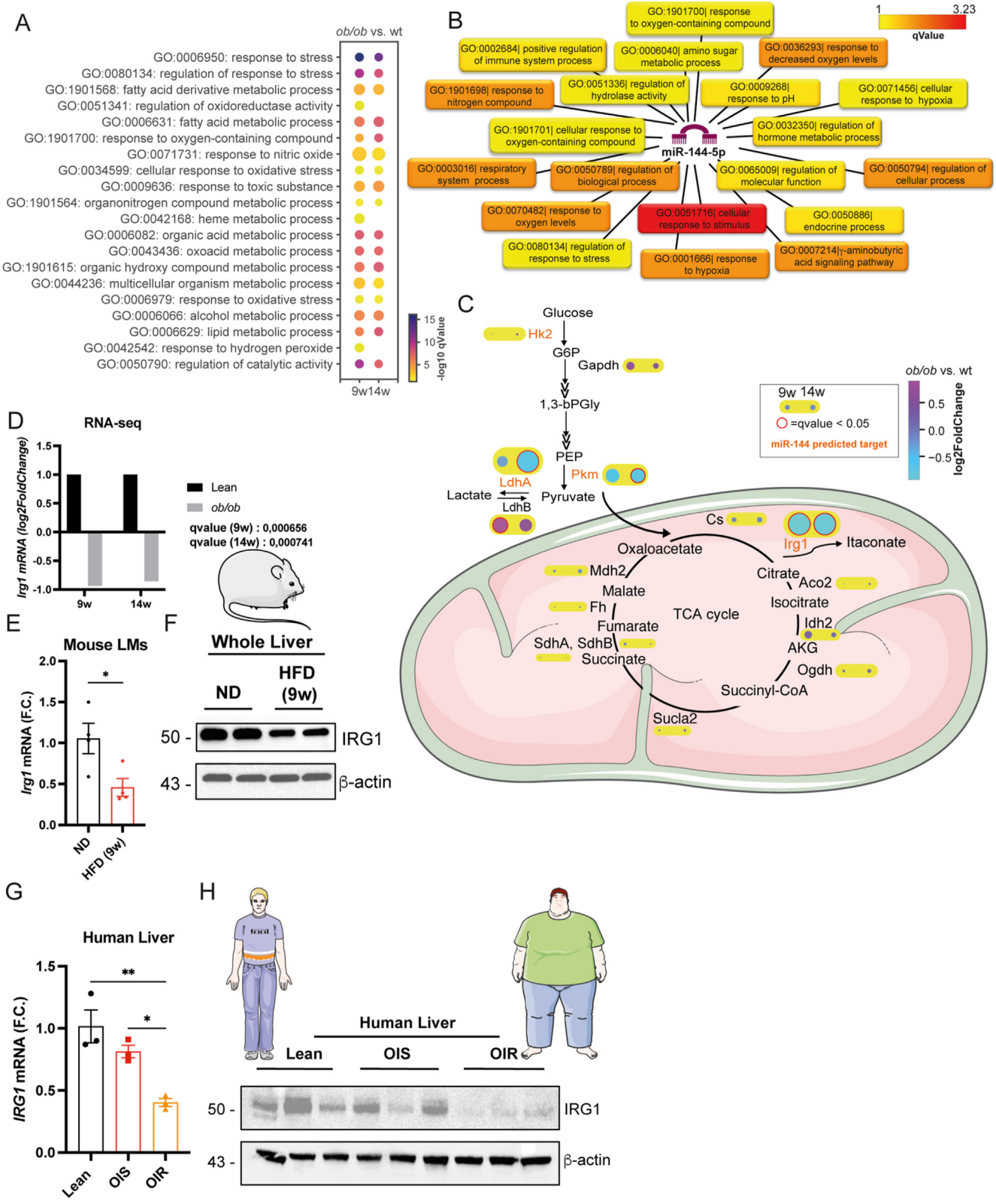

measures nascent transcripts, revealed that, in mice fed an HFD, LMs actively respond to obesity-induced metabolic stress (see Supplementary Figure 1*B*). In line with in silico analyses, intracellular ROS levels were upregulated in HFD mice compared with lean controls (see Supplementary Figure 1*C*). Considering the intricate relationship between oxidative stress and cellular metabolism and the importance of miR-144 as regulator of hepatic endogenous antioxidant response[22] during obesity, we investigated miR-144 contribution to energy metabolism. GO enrichment analysis for significantly downregulated miR-144 predicted targets in LMs of *ob/ob* mice at both 9 and 14 weeks confirmed miR-144 role in the regulation of obesity-induced metabolic stress (Figure 1*B*).

To further identify which metabolic pathways could potentially be regulated in obesity by miR-144, we analyzed the expression of miR-144 metabolic target genes. We found *Acod1* encoding the immunoresponsive gene 1 (*Irg1*) enzyme as the only significantly downregulated gene in obese mice at both ages (Figure 1*C* and *D*). Consistently, RNA-seq, quantitative polymerase chain reaction and western blot confirmed that both *Irg1* mRNA and protein levels were decreased on high-fat feeding in mouse LMs and whole livers, where miR-144 is upregulated[22] (Figure 1*E* and *F*). *Irg1* reduction was combined with hepatic ROS upregulation in obese mice, corroborating the sustained metabolic and oxidative stress previously reported in these mice[22] (Supplementary Figure 1*C* and *D*). Predictive in silico target analysis showed miR-144 seed region pairing with the 3′ untranslated region of Irg1 (see Supplementary Figure 1*E*), supporting *Irg1* as a direct target of miR-144.

Because of the conserved role of miR-144 in the regulation of the antioxidant response in mice and humans,[22]we measured *IRG1* in human liver biopsies of lean, obese insulin-sensitive and obese insulin-resistant individuals. Similar to mice, *IRG1* mRNA and protein levels were downregulated in obesity and insulin resistance, in which miR-144 expression is increased[22] (Figure 1*G* and *H*). Altogether, these data suggested that the miR-144–predicted target *IRG1* is downregulated during obesity in mice and humans.

TCA Cycle Enzymes Succinate Dehydrogenase and FH Are Hyperactivated in Obesity

IRG1 catalyzes the production of the metabolite itaconate, which has been described as an inhibitor of succinate dehydrogenase (SDH) in macrophages.[38] SDH converts succinate to fumarate and we therefore measured the SDH activity, and the levels of succinate and fumarate in the liver of obese mice fed an HFD compared with lean. As miR-144 is highly expressed in both LMs and hepatocytes,[22] these analyses were performed in the whole liver. Consistent with previous studies,[39–42] specific assays demonstrated that citrate and SDH activity were increased in mice fed an HFD (Figure 2*A* and *B*). As expected, SDH activation on obesity led to the consumption of its substrate succinate (Figure 2*C*). Unexpectedly, we found fumarate levels also decreased on obesity (Figure 2*D*). Therefore, we measured the activity of FH, the enzyme responsible for the conversion of fumarate to malate. Consistently, FH activity was upregulated in obese mice (Figure 2*E*), whereas malate levels remained unchanged (Figure 2*F*). Similarly, citrate and both SDH and FH activities were upregulated in livers of obese insulin-resistant patients compared with obese insulin-sensitive and lean individuals, reflected by reductions of succinate and fumarate (Figure 2*G*–*K*), without affecting malate (Figure 2*L*). These data suggested that *Irg1* reduction in obesity is associated with the selective hyperactivation of both SDH and FH, subsequently reducing succinate and fumarate in mice and humans (Figure 2*M*).

miR-144 silencing Is Associated With Decreased SDH and Fumarase Activities

To investigate the role of miR-144 as regulator of *Irg1* and the TCA cycle in vivo, we used glucan-encapsulated RNA interference particles (GeRPs)[9,35] to deliver small interfering RNA (siRNA) specifically to LMs. As we have previously shown,[22] specific silencing of miR-144 in LMs results in ROS scavenging, ameliorating the whole liver microenvironment. GeRP-mediated silencing of miR-144 increased *Irg1* expression in LMs (Figure 3*A*), hepatocytes (Figure 3*B*), and livers (Figure 3*C*) of mice fed an HFD. These results confirmed *Irg1* mRNA as a miR-144 direct target in murine liver.

Tissue digestion and cell isolation could dramatically impact cellular metabolism.[39] Therefore, to assess miR-144 silencing effect on the TCA cycle in LMs within their native microenvironment, we used a histochemistry-based technique that allows visualization and quantification of specific enzymatic activities on single cells. Using fluorescein isothiocyanate–labeled GeRPs, we analyzed the activity of key enzymes of the TCA cycle and glucose metabolism in

Figure 1. miR-144 predicted target *Irg1* is downregulated in obese-induced insulin-resistant livers. (*A*) Selected significantly enriched GO biological processes of genes differentially expressed in 9- and 14-week-old LMs of *ob/ob* mice compared with WT mice (n = 4 WT, n = 3 *ob/ob* for 9 weeks; n = 4 for 14 weeks) based on RNA-seq data. The full list of significant biological processes is in Supplementary Tables 2 and 3. (*B*, *C*) Predicted cellular metabolism-associated (*B*) and related to glycolysis and TCA cycle (*C*) biological processes targeted by miR-144–5p in *ob/ob* mice. Full list of overrepresented GO biological processes is in Supplementary Tables 4 and 5. (*D*) RNA-seq-data-based *Irg1* expression of 9- and 14-week-old WT and *ob/ob* mice (n = 4 WT, n = 3 for *ob/ob* at 9 weeks; n = 4 for *ob/ob* 14 weeks). (*E*, *F*) *Irg1* mRNA (*E*) or protein (*F*) in LMs or whole livers of mice fed an HFD or normal diet (ND) for 9 weeks (n = 3 per condition). (*G*, *H*) *IRG1* mRNA (*G*) or protein (*H*) in lean, obese insulin-sensitive (OIS) and obese insulin-resistant (OIR) human individuals (n = 3 per condition). Data are means ± SEM. $^{*}P < .05$, $^{**}P < .01$, $^{***}P < .001$

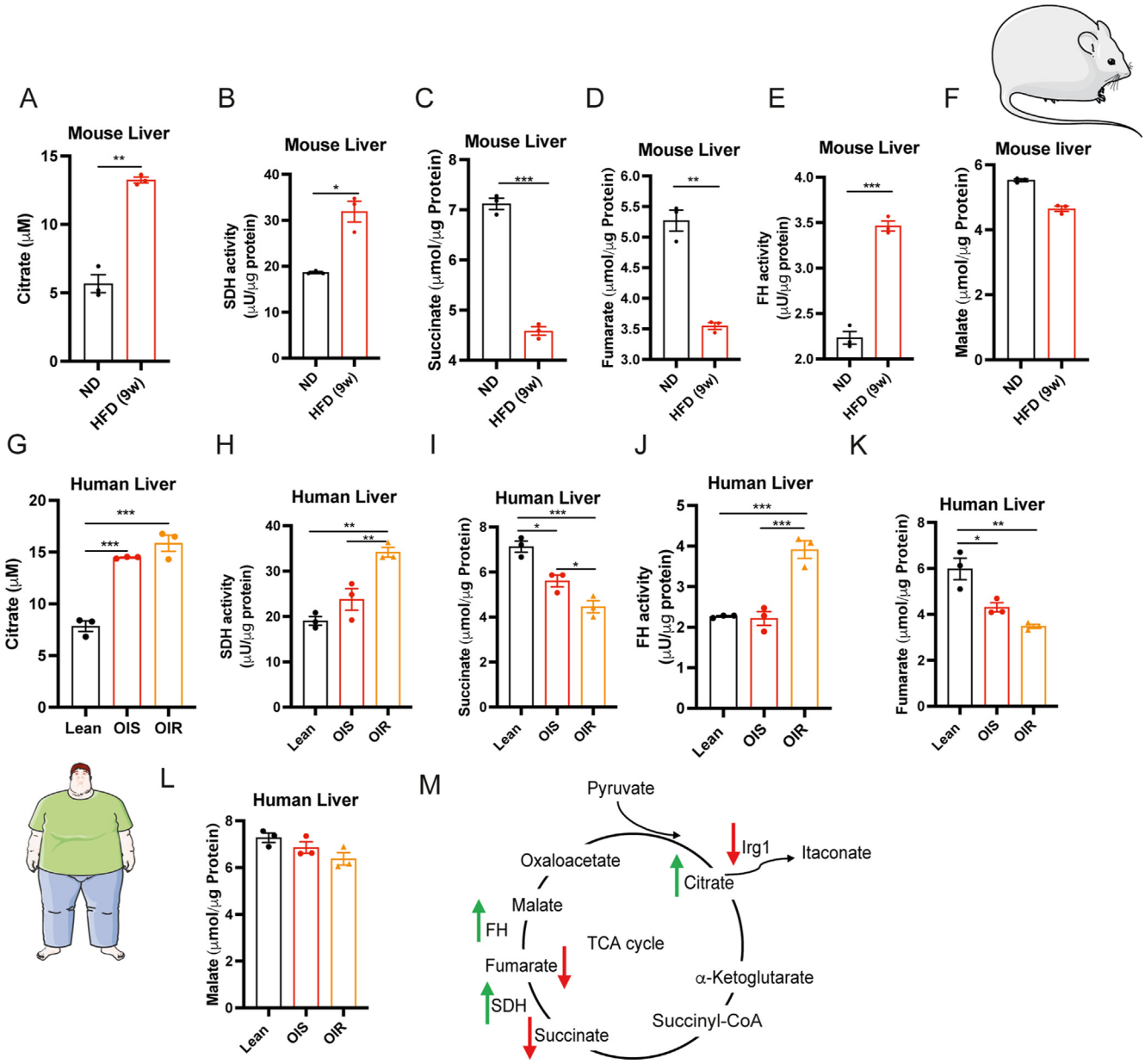

Figure 2. TCA cycle enzymes. SDH and FH are hyperactivated in obesity. (*A–F*) Citrate (*A*), SDH activity (*B*), succinate (*C*), FH activity (*D*), fumarate (*E*), and malate (*F*) in whole livers from mice fed an HFD or normal diet (ND) for 9 weeks. (*G–L*) Citrate (*G*), SDH activity (*H*), succinate (*I*), FH activity (*J*), fumarate (*K*), and malate (*L*) in lean, obese insulin-sensitive (OIS) and obese insulin-resistant (OIR) human individuals. (*M*) Proposed model for *Irg1* downregulation effect on TCA cycle enzymes upon obesity. n = 3 per condition. Data are means ± SEM. **P* < .05, ***P* < .01, ****P* < .001.

GeRP-amiR-144 or GeRP-scr-treated LMs. miR-144 knockdown significantly reduced SDH activity in cells in situ (Figure 3*D*), whereas lactate dehydrogenase, glucose-6-phosphate dehydrogenase, and isocitrate dehydrogenase activities were not influenced (see Supplementary Figure 2*A–C*). Additional activity assays confirmed decreased SDH, and succinate accumulation, on miR-144 silencing in the whole liver (Figure 3*E* and *F*). Interestingly, we also observed that GeRP-amiR-144 blunted FH activity (Figure 3*G*), increasing fumarate levels (Figure 3*H*). These results suggested that miR-144 silencing selectively affects the activities of SDH and FH in vivo.

To test the ability of miR-144 to silence *IRG1* in human liver cells, we treated NPCs with a miR-144 mimic (see Supplementary Figure 2*D*), which significantly downregulated *IRG1* mRNA levels (Figure 3*I*), confirming IRG1 as a conserved miR-144 target in humans. Thereafter, to explore whether miR-144 could directly regulate SDH and FH in humans, we analyzed their activities in NPCs following overexpression of miR-144, as observed during obesity. Similar to mice, mimic-miR-144 treatment increased SDH and FH activities in NPCs (Figure 3*J*), suggesting that, in both mice and humans, miR-144 could regulate both SDH and FH (Figure 3*K*).

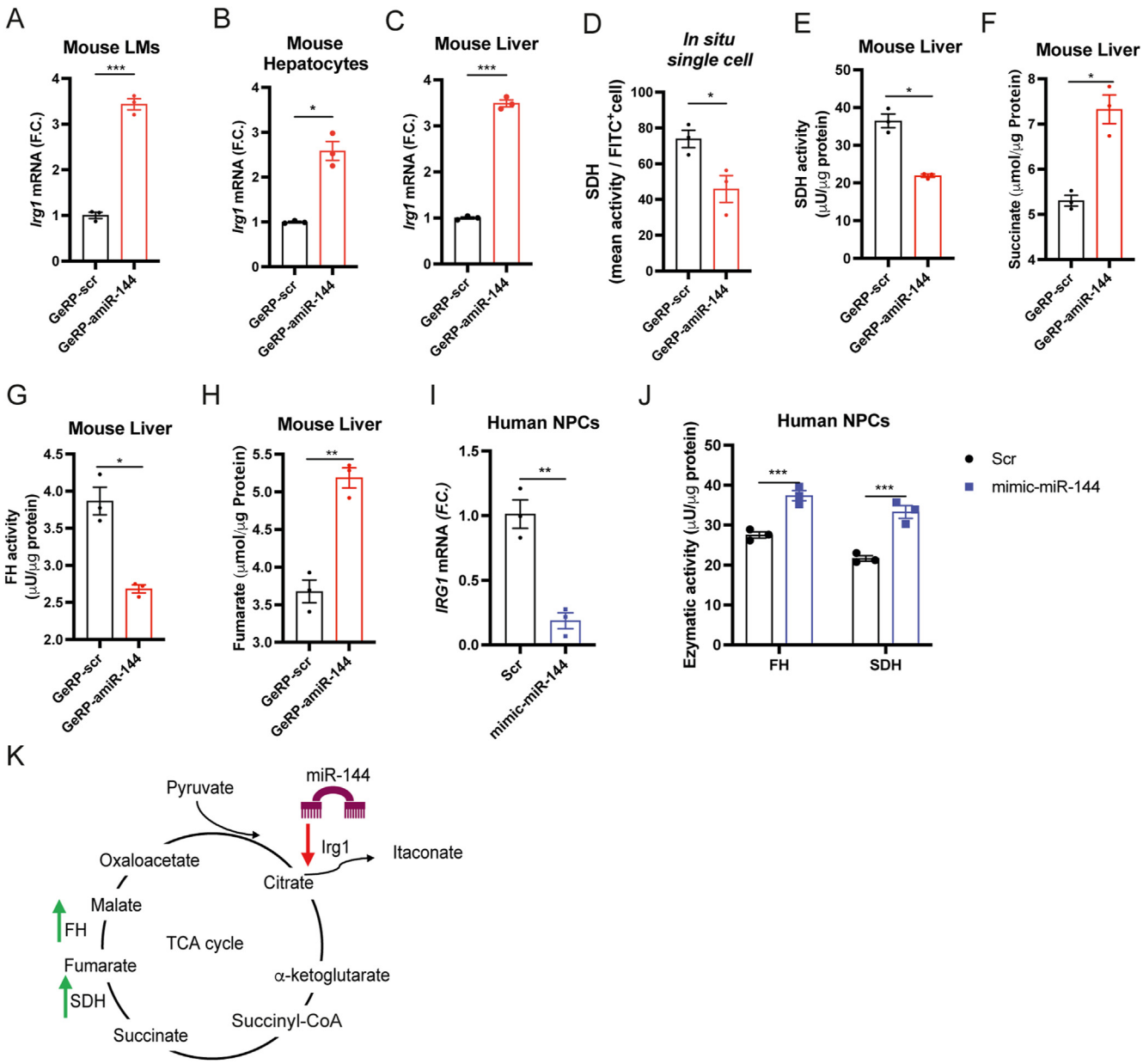

Figure 3. miR-144 silencing is associated with decreased succinate dehydrogenase and fumarase activities. (*A–C*) *Irg1* mRNA in LMs (*A*), hepatocytes (*B*), and whole livers from GeRP-scrambled control (scr)- and GeRP–amiR-144–treated mice. (*D*, *E*) SDH activity using in situ single-cell enzyme histochemistry analysis (*D*) and specific enzymatic assay (*E*) in whole livers from GeRP-scr and GeRP–amiR-144–treated mice. (*F–H*) Succinate (*F*), FH activity (*G*), and fumarate (*H*) in whole livers from GeRP-scr and GeRP–amiR-144–treated mice. (*I*) miR-144 in human NPCs untreated or treated with mimic-miR-144 (n = 3 per condition). (*J*) SDH and FH activity in human NPCs untreated or treated with mimic-miR-144. (*K*) Proposed model for miR-144 direct targeting of *Irg1* upon obesity. n = 3 per condition. Data are means ± SEM. **P* < .05, ***P* < .01, ****P* < .001.

Irg1 Silencing by miR-144 Increases SDH and FH Activities in Obesity

To test whether *IRG1* was involved in miR-144–driven regulation of SDH and FH, we analyzed their activities following treatments to increase or silence miR-144 or *IRG1* in NPCs. As previously shown, treatment of NPCs with free fatty acids (FFAs), to mimic the excessive hepatic lipid accumulation observed in obesity,[22] increases miR-144 levels, which in turn silence *IRG1* (Figure 4*A* and *B*). Moreover, FFAs increased both SDH and FH activities (Figure 4*C* and *D*, first 2 graphs). miR-144 silencing inhibited the effect of FFAs on SDH and FH activities (Figure 4*C* and *D*, third graph). Not surprisingly, silencing *IRG1* did not affect the enzymes, because *IRG1* expression is already strongly downregulated by the upregulation of miR-144 driven by FFAs. To functionally test the relationship between *IRG1* expression and SDH inhibition, we used lipopolysaccharide (LPS) treatment.[43–45] As expected, LPS increased *IRG1* expression without affecting miR-144 levels (see

Supplementary Figure 2*E* and *F*). Interestingly, silencing *IRG1* by treating NPCs either with an miR-144 mimic or using an siRNA targeting *IRG1* blocked the effect of LPS on SDH and FH (Figure 4*E* and *F*), highlighting the importance of *IRG1* in the miR-144–dependent regulation of SDH and FH.

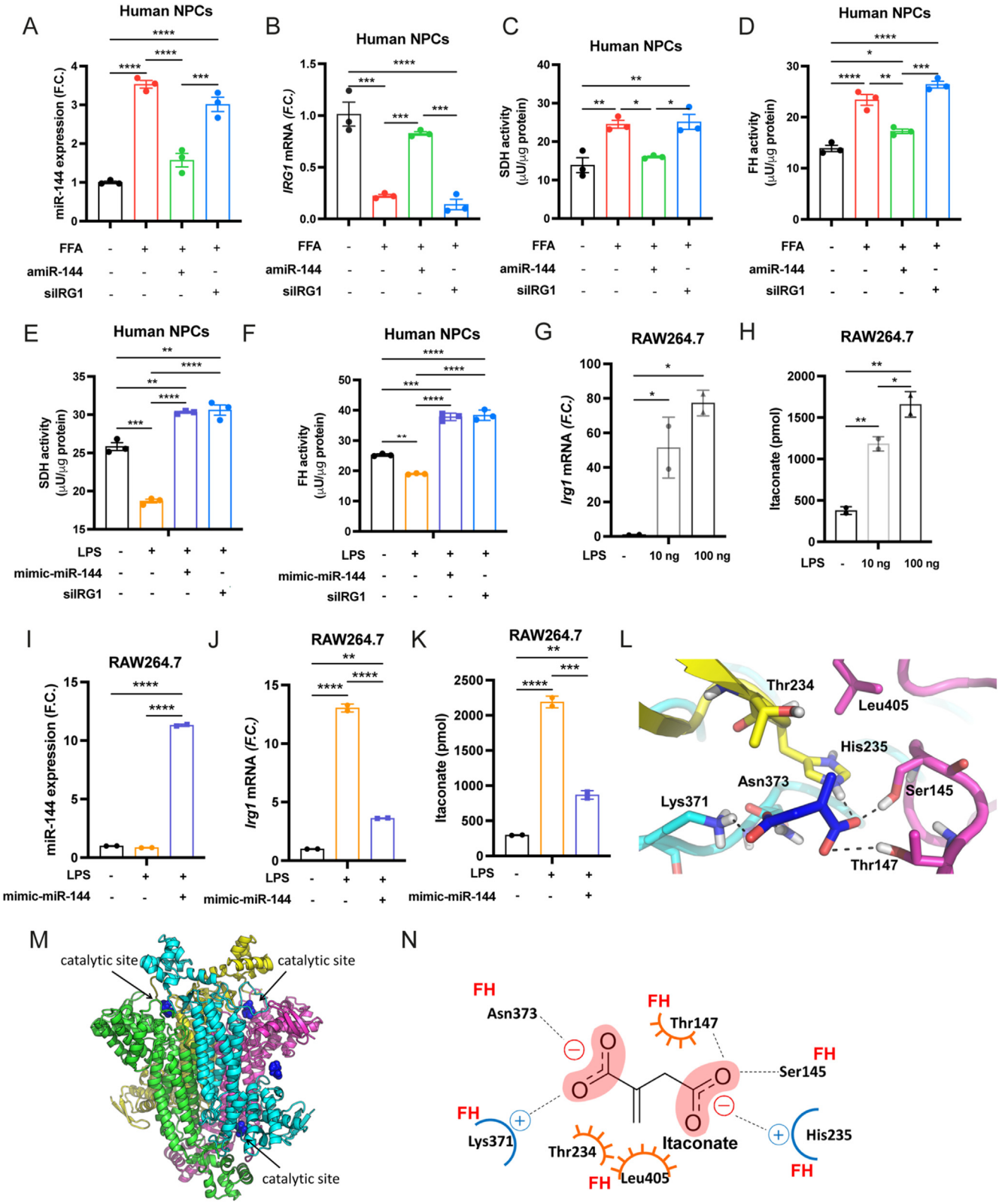

To test whether miR-144 silencing of *Irg1* was associated with a reduction in itaconate, we used an in vitro model of RAW 264.7 cells treated with LPS.[38,45,46] As expected, *Irg1* expression and itaconate production were significantly increased by LPS treatment (Figure 4*G* and *H*), whereas miR-144 expression was not affected. miR-144 overexpression significantly decreased *Irg1* expression and the production of itaconate induced by LPS (Figure 4*I*–*K*), providing a proof-of-principle that miR-144 could silence the expression of *Irg1* and reduce itaconate production. These data were in line with the previous studies,[38,45,47–49] reporting, in LPS-activated macrophages, an inhibitory role of *IRG1* toward SDH via itaconate; however neither *IRG1* nor itaconate had ever been implicated in the regulation of fumarase.

Fumarase catalyzes the reversible stereospecific hydration of fumarate to L-malate and is assembled in a homotetramer.[50] Interestingly, itaconate structure is highly similar to both succinate and fumarate (See Supplementary Figure 2*G*), suggesting a possible competitive role in binding both SDH and FH. To investigate itaconate affinity to FH, and to provide insights into its possible binding site, we simulated the intermolecular recognition and binding processes of itaconic acid to the homo-tetrameric FH by molecular dynamics (MD) simulations. MD is a computer-aided simulation allowing the analysis of movements of atoms and molecules within time, providing a dynamic snapshot of molecular systems. Here, 4 molecules of itaconate were randomly placed in the solvent area at a distance higher than 20 Å from the FH surface, and the system was simulated for 500 ns by MD with no constraints. Notably, results show itaconate has high propensity to bind to FH. Specifically, 3 itaconate molecules bind within the FH catalytic site in close contact to residues Ser145, Thr147, His235, Lys371, Asn373, and in proximity to Thr234 and Leu405 (Figure 4*L*–*N*). The fourth molecule binds to a different no active site, in contact to Arg87 and Asn133 (see Supplementary Figure 2*H*). To provide further details into the theoretical affinity of itaconate for the 2 FH binding sites, Molecular Mechanics Poisson-Boltzmann Surface Area calculations were carried out. Results are listed in Table 1 and show itaconate stronger theoretical affinity for the catalytic site identified by MD simulations. Altogether, these results suggest that *IRG1* and presumably itaconate could inhibit not only SDH but also FH in human and murine liver cells.

Table 1. Theoretical affinity of itaconate to FH.

Molecule/binding site	Delta energy of binding (MM-PBSA) kcal/mol ± SEM
Itaconate #1/catalytic site	-11.29 ± 1.42
Itaconate #2/catalytic site	-12.16 ± 0.94
Itaconate #3/catalytic site	-12.49 ± 1.63
Itaconate #4/additional site	-5.86 ± 0.93

Exogenous Itaconate Inhibits FH Activity and the Consumption of Fumarate in Human NPCs

To investigate further whether itaconate could directly inhibit FH in vitro, we studied the kinetics of the miR-144–driven reduction in SDH and FH activities in NPCs following FFA treatment. FFAs increased the activity of both SDH and FH in NPCs, whereas 4-octyl itaconate (4-OI) administration significantly reduced their activities (Figure 5*A* and *B*). Importantly, FH activity reduction was observed 2 minutes after 4-OI treatment (Figure 5*A*), whereas SDH activity started to decrease after 3 minutes (Figure 5*B*). These results suggest that itaconate could indeed inhibit FH activity through competition with its substrate, resulting in fumarate accumulation that subsequently reduced SDH activity.

We then analyzed the immunometabolic effect of 4-OI on human NPCs on miR-144 overexpression. As expected, 4-OI did not change *IRG1* mRNA, which was strongly downregulated following treatment with miR-144 mimic (Figure 5*C* and Supplementary Figure 3*A*). miR-144 overexpression in human NPCs increased the activity of SDH and FH (Figure 5*D* and *E*, magenta lines), with consumption of both succinate and fumarate (Figure 5*F* and *G*, first 2 graphs). Strikingly, 4-OI administration counteracted miR-144 effect on SDH and FH (Figure 5*D* and *E*, green and orange lines), restoring succinate and fumarate (Figure 5*F* and *G*, last graph) to basal levels. Importantly, other metabolites, such as citrate and malate, were not affected by 4-OI treatment (see Supplementary Figure 3*B* and *C*), highlighting the specificity of itaconate axis for succinate and fumarate branches of the TCA cycle. Altogether, these data suggest a pivotal role of *IRG1*, and presumably itaconate, in the regulation of SDH and FH activities during obesity.

Figure 4. *IRG1* silencing by miR-144 increases SDH and FH activities in the obese state. (*A*, *B*) miR-144 (*A*) and *IRG1* mRNA (*B*) in human NPCs untreated, treated with FFAs and with scr, amiR-144 or after silencing *Irg1* (siIRG1, n = 3 per condition). (*C*, *D*) SDH (*C*) and FH (*D*) activity in human NPCs untreated, treated with FFAs and with scr, amiR-144, or after silencing *Irg1* (siIRG1, n = 3 per condition). (*E*, *F*) SDH (*E*) and FH (*F*) activity in human NPCs untreated, treated with LPS and with scr, mimic-miR-144 or after silencing *Irg1* (siIRG1, n = 3 per condition). (*G*) *Irg1* mRNA in murine RAW264.7 cells untreated and treated with 10 or 100 ng of LPS (n = 2 technical replicate from 2 million pooled cells). (*H*) Itaconate intracellular levels in murine RAW264.7 cells untreated and treated with 10 or 100 ng of LPS (n = 2 technical replicate from 2 million pooled cells). (*I*, *J*) miR-144 (*I*) and *Irg1* mRNA (*J*) in murine RAW264.7 cells untreated and treated with LPS or mimic-miR-144 (n = 2 technical replicate from 2 million pooled cells). (*K*) Itaconate intracellular levels in murine RAW264.7 cells untreated and treated with LPS, scr, or mimic-miR-144 (n = 2 technical replicate from 2 million pooled cells). (*L*) Binding model of itaconate within the catalytic site of FH as predicted by MD simulations. (*M*) Representative structure (most populated cluster, with a population of 74% of MD frames) extracted from MD trajectories. (*N*) Main interactions established by itaconate within the FH catalytic site, by MD simulations. Data are means ± SEM and ± SD for (*G*–*K*). **P* < .05, ***P* < .01, ****P* < .001, and *****P* < .0001.

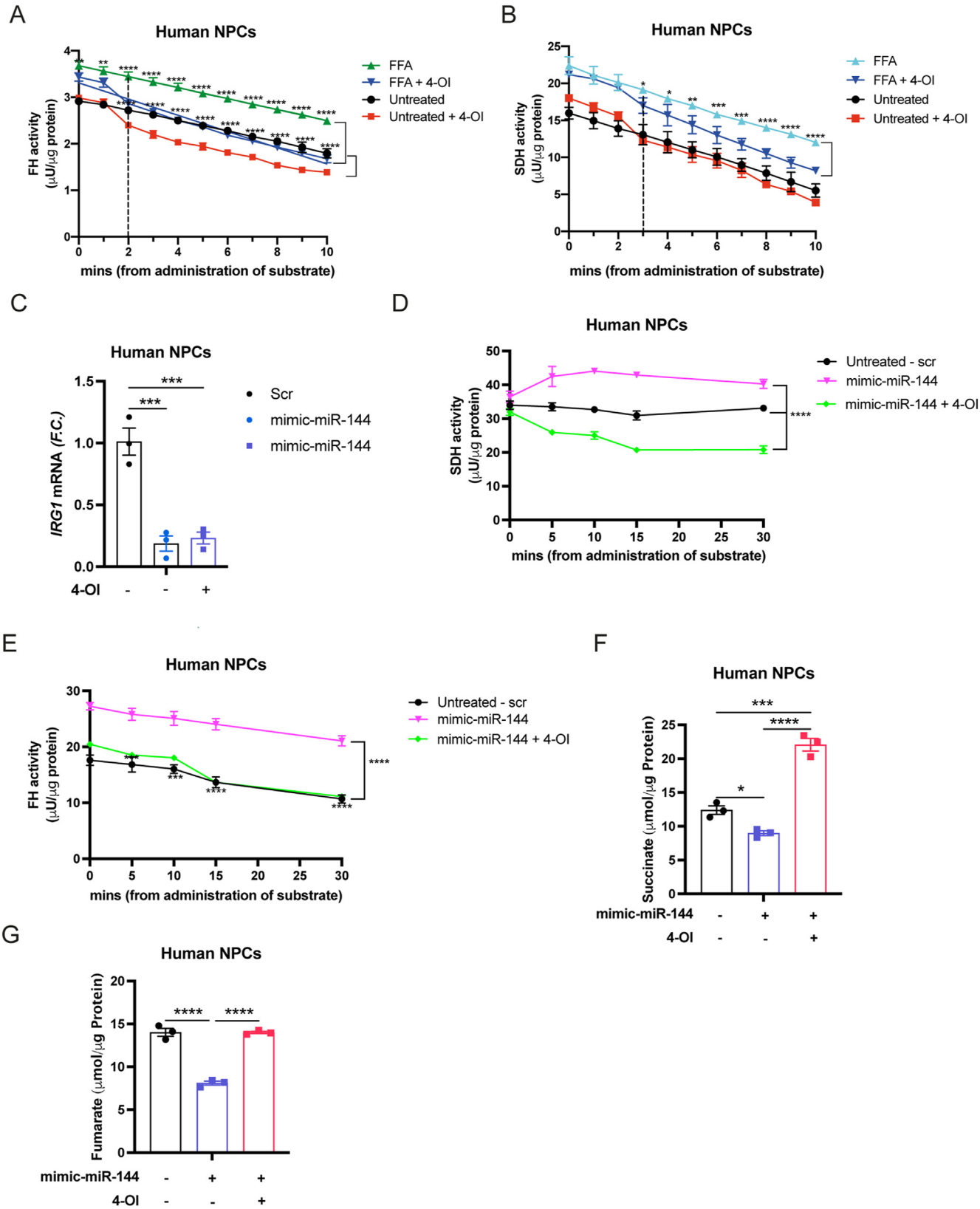

Figure 5. Exogenous itaconate inhibits FH activity and the consumption of fumarate in human NPCs. (*A*, *B*) Kinetics assays for FH (*A*) and SDH (*B*) activities in human NPCs untreated or incubated with FFA and treated with 4-OI. (C) miR-144 in human NPCs treated with scr, mimic-miR-144, and/or 4-OI. (*D*, *E*) Kinetics assays for SDH (*D*) and FH (*E*) activities in human NPCs treated with scr, mimic-miR-144, and/or 4-OI .(*F*, *G*) Succinate (*F*) and fumarate (*G*) in human NPCs treated with scr, mimic-miR-144, and/or 4-OI. n = 3 per condition. Data are means ± SEM. *$P < .05$, **$P < .01$, ***$P < .001$, and ****$P < .0001$.

miR-144 Decreases NRF2 Activity Via Fumarate Reduction in Obesity

We have previously reported that silencing miR-144 in LMs of obese mice restored the levels of NRF2 and the antioxidant defense.[22] Because IRG1-driven SDH inhibition in LPS-activated macrophages has been proposed to encompass an anti-inflammatory role,[43] here we measured the inflammatory cytokine *Tnf-α* following miR-144 knockdown. In our model, miR-144 silencing did not influence *Tnf-α* expression (see Supplementary Figure 4*A*), indicating that the inhibitory effect of IRG1 on SDH was occurring independently of inflammatory stimuli. Consistently, our previous studies demonstrated that during obesity, human and murine LMs developed oxidative stress independently of inflammation.[9] We have previously demonstrated, in liver spheroids, that FFAs could mimic hepatic steatosis, inducing miR-144 and oxidative stress.[22] To study the effects of miR-144 silencing on *IRG1* expression and cellular metabolism in this human model of obesity, we used 4 types of liver spheroids: those with basal miR-144 expression in both hepatocytes and NPCs, those with miR-144 silenced only in NPCs or only in hepatocytes, and those with miR-144 silenced in both populations (Figure 6*A*). FFA treatment reduced the expression of *IRG1* in liver spheroids, which was completely reversed by miR-144 silencing (Figure 6*B*). These results corroborated the hypothesis that miR-144 reduces hepatic *IRG1* expression in human obese individuals. We next tested whether the increase of *IRG1* following miR-144 silencing could also impact SDH and FH activities as observed in mouse models. As expected, both FH and SDH activities were decreased, accumulating fumarate and succinate (Figure 6*C*–*F*), independently of *TNF-α* expression levels (see Supplementary Figure 4*B*).

Given that fumarate activates NRF2, destabilizing the protein complex CUL3-KEAP1 (Figure 6*G*), we measured KEAP1, CUL3, and NRF2 activity following miR-144 silencing in liver spheroids. Immunoprecipitation experiments displayed a strong decrease in CUL3 associated to KEAP1 on miR-144 silencing (Figure 6*H*). As previously described,[22] KEAP1 was not affected by miR-144 knockdown. However, NRF2 activity was increased on miR-144 silencing as measured by the levels of phosphorylation on Serine 40 and the expression of NRF2 target genes *GSTP1, CES2G,* and *HMOX1* (Figure 6*I*).

Because our previous studies demonstrated that miR-144 targeted NRF2 total protein levels,[22] here we investigated whether miR-144 could also influence NRF2 protein levels and activation, via direct targeting of *IRG1*. To address this, we silenced either miR-144 or *IRG1* individually in NPCs and measured NRF2 phosphorylation and protein levels in cells treated with FFA. NRF2 protein levels, normalized to β-actin, were decreased on miR-144 silencing but were not affected by *IRG1* knockdown. Although these results suggested that miR-144 could regulate total NRF2 protein independently of IRG1 (see Supplementary Figure S4*C*, first 2 graphs), IRG1 levels were already strongly downregulated by treatment with FFA. Interestingly, phosphorylation of NRF2, normalized to total NRF2, was not affected by miR-144 but decreased on IRG1 silencing (see Supplementary Figure 4*C*, last graph). This resulted in the inhibition of NRF2 antioxidant response on *IRG1* knockdown, which was completely rescued by miR-144 silencing, as demonstrated by quantitative polymerase chain reaction for NRF2 target gene *NQO1* (see Supplementary Figure 4*D*). To further elucidate the role of IRG1 in NRF2 regulation by miR-144, we overexpressed miR-144 in human NPCs and rescued IRG1 by LPS treatment. Rescuing *IRG1* completely restored NRF2 protein levels (see Supplementary Figure 4*E* and *F*) and increased *NQO1* expression (see Supplementary Figure 4*G*). All these data suggested that miR-144 regulates NRF2 protein levels and activity via IRG1.

Discussion

In this study, we investigated the role of miR-144 in the regulation of mitochondrial metabolism and NRF2 activity in the livers of obese insulin-resistant humans and mice. Although the association among mitochondrial dysfunction, oxidative stress, and obesity progression has been extensively studied,[15,51–54] mitochondrial function in macrophages in metabolic diseases remains largely unknown. Herein, transcriptomic profiling revealed a profound alteration of the energetic metabolism in LMs from obese mice.

We found that in obese mice and humans, hepatic miR-144 targets *Irg1*, a gene encoding the enzyme IRG1, which catalyzes itaconate formation. Itaconate has been previously proposed, given its structural similarity with succinate, as an anti-inflammatory metabolite involved in the remodeling of LPS-treated macrophages via inhibition of the SDH enzyme.[38,45,55,56] Consistently, the downregulation of *IRG1* in obese livers was associated with an increased activity of SDH, resulting in the excessive consumption of its substrate succinate. Although these results were in line with previous reports in LPS-primed macrophages,[38] LMs do not undergo inflammatory activation during obesity.[9] However, recent findings described itaconate as a immunomodulatory rather than purely anti-inflammatory metabolite.[49] Therefore, miR-144 regulation of *Irg1*-mediated inhibition of SDH could occur independently of inflammation. Consistent with this hypothesis, silencing of miR-144 in LMs of obese mice and human spheroids increased *IRG1* expression and decreased SDH activity without affecting the proinflammatory cytokine *TNF-α*. In addition, the activity of glycolytic enzymes glucose-6-phosphate dehydrogenase and lactate dehydrogenase was not affected by miR-144 knockdown. Considering that increased glycolysis is a hallmark of macrophage activation in response to inflammation,[57,58] we confirmed that during obesity LMs undergo a metabolic rewiring independently of their inflammatory status.[9] Strikingly, also FH activity was decreased following miR-144 silencing in obese mice and in human NPCs or liver organoids. Interestingly, LPS treatment inhibited both SDH and FH in NPCs. This suggested that itaconate could also inhibit FH activity, conceivably due to its structural similarity with FH

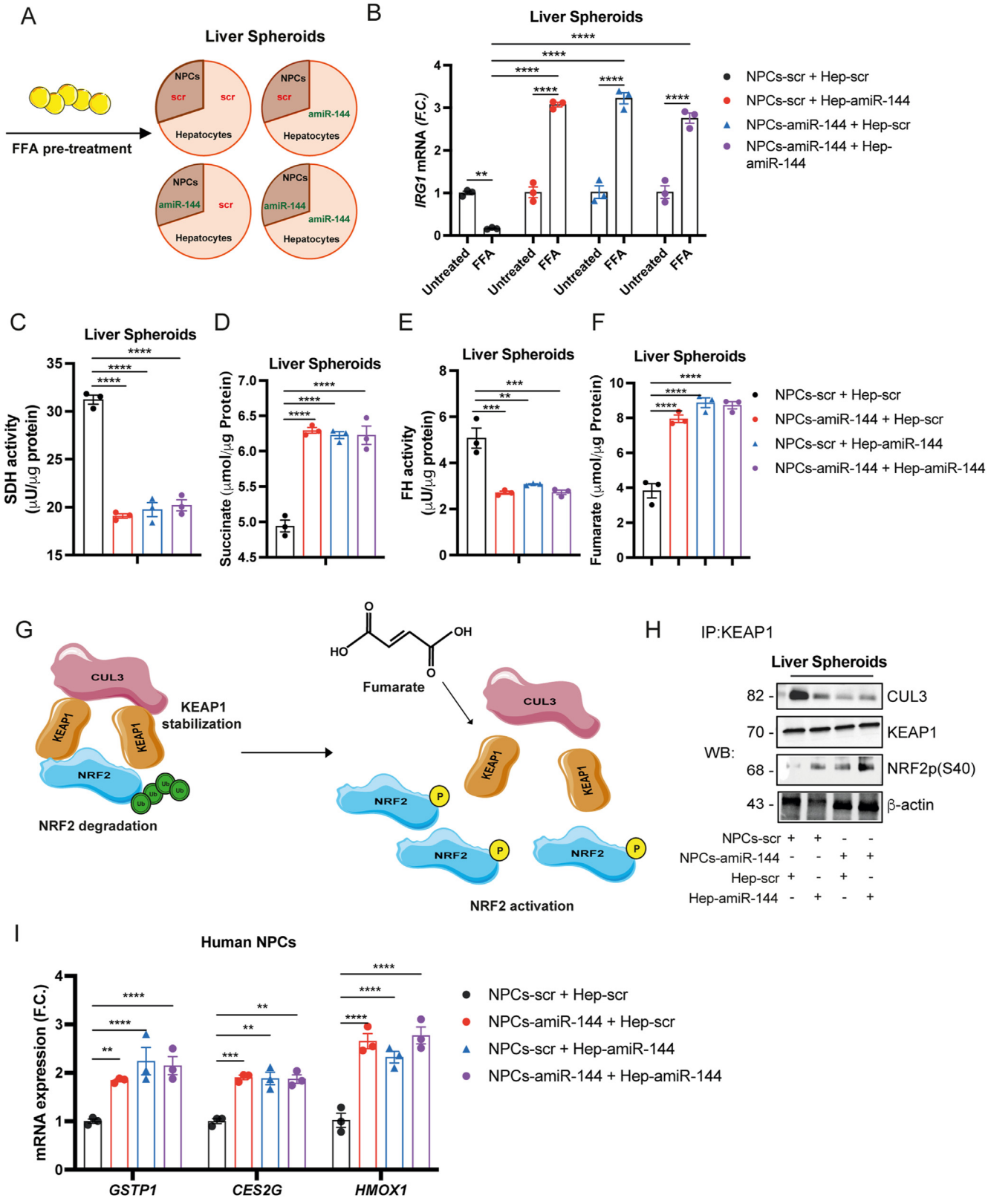

Figure 6. miR-144 decreases NRF2 stability via fumarate reduction in obesity. (*A*) Liver spheroid organization. (*B*) *IRG1* mRNA in FFA-exposed human liver spheroids treated with amiR-144 or scr. (*C–F*) SDH activity (*C*), succinate (*D*), FH activity (*E*), and fumarate (*F*) in FFA-exposed human liver spheroids treated with amiR-144 or scr. (*G*) NRF2 activity regulation by fumarate. (*H*) Western blot of CUL3, KEAP1, and NRF2 phosphorylation on Serine40 after immunoprecipitation of KEAP1 in FFA-exposed human liver spheroids treated with amiR-144 or scr. (*I*) Reverse transcription quantitative polymerase chain reaction analysis of *GSTP1, CES2G,* and *HMOX1* mRNA in FFA-exposed human liver spheroids treated with amiR-144 or scr. n = pooled liver spheroids from 3 human donors. Data are means ± SEM. $^{*}P < .05$, $^{**}P < .01$, $^{***}P < .001$, and $^{****}P < .0001$.

substrate fumarate. The active FH enzyme is a homotetramer,[59] and our modeling analysis revealed that itaconate may bind the catalytic sites of FH with high thermodynamic affinity. Itaconate could therefore compete with fumarate and inhibit FH. In support of this finding, our study showed that administration of 4-OI to human NPCs results in decreased FH activity preceding the inhibition of SDH. In addition, we demonstrated that miR-144 overexpression in human NPCs, a condition that is similar to obesity, increased both SDH and FH activities. However, exogenous administration of 4-OI was sufficient to restore both enzyme levels, thus confirming that miR-144 regulates FH and SDH activities through specific silencing of *IRG1*, presumably reducing itaconate production.

The conversion of 4-OI to itaconate has recently been debated[49,60] and therefore we cannot completely exclude that the inhibitory effect on FH and SDH is specific for 4-OI and not for itaconic acid per se. However, the similarity between 4-OI and itaconate structures and the results of our MD simulations performed using itaconate as a template strongly suggest that endogenous itaconate might indeed compete with fumarate to bind FH catalytic site. IDH, if inhibited, could potentially redirect aconitate to itaconate production[61]; however, miR-144 silencing did not affect the measured activity of isocitrate dehydrogenase 3, suggesting regulation specifically through *IRG1* and not due to buildup of aconitate. It has also been demonstrated that in certain conditions (ie, hypoxia), IRG1 levels were not related to itaconate production, potentially due to differences in substrate availability or posttranslational modification of the enzyme.[44] Although we were not able to detect measurable levels of itaconate in NPCs because additional work is needed to develop the optimum methodology to measure itaconate in our model of primary cells, *IRG1* is a widely accepted "biosensor" of intracellular itaconate levels.[47,48] However, we provided the proof-of-principle that miR-144 decreases both *Irg1* expression and itaconate production on stimulation of RAW 264.7 cells with LPS. We therefore hypothesized that the downregulation of *Irg1* by miR-144, which is increased in obese livers, reduces itaconate levels. In line with this hypothesis, treatment with 4-OI blocked the effect of miR-144–driven *IRG1* silencing on SDH and FH activation.

FH is crucial for intracellular energetic metabolism and, interestingly, its downregulation in adipose tissue has a protective effect in obese insulin-resistant mice.[62] In line with these results, FH inhibition following miR-144 silencing in obese mice and human liver spheroids, increased NRF2 levels and activity and reduced oxidative stress, upregulating NRF2 target genes *GSTP1, CES2G, HMOX1,* and *NQO1*. Here we propose the hypothesis that itaconate-mediated inhibition of FH activity could be protective in the lean/obese insulin-sensitive liver, regulating the TCA cycle in redirecting metabolites to drive NRF2 signaling. In the insulin-resistant state, miR-144 upregulation attenuates this protective response.

Herein, we found that upon obesity, miR-144 knockdown restored *Irg1* and fumarate levels. This condition led to the decreased binding of KEAP1 to CUL3, an ubiquitin-ligase that mediates NRF2 polyubiquitination and degradation,[63–65] increasing the phosphorylation of NRF2, which is a marker of its activity.[65] Interestingly, dimethyl fumarate, a stable form of fumaric acid, has been proposed as a treatment for oxidative stress–related diseases.[33,66–70] However, given the adverse side effects associated with dimethyl fumarate administration,[71] miR-144 modulation could be used as a novel strategy to regulate endogenous fumarate intracellular levels and NRF2 activity.

In summary, this study unravels the crucial role of miR-144 as regulator of hepatic metabolism and TCA cycle in obesity-induced insulin resistance in mice and humans. Herein, we demonstrated that miR-144 regulates NRF2 levels by targeting *IRG1* via the accumulation of fumarate. Given its role in the regulation of NRF2-mediated antioxidant response, targeting hepatic miR-144 could possibly represent a novel therapeutic approach in the treatment of metabolic diseases.

Supplementary Material

Note: To access the supplementary material accompanying this article, visit the online version of *Gastroenterology* at www.gastrojournal.org, and at https://doi.org/10.1053/j.gastro.2021.08.030.

References

1. Kahn SE, Hull RL, Utzschneider KM. Mechanisms linking obesity to insulin resistance and type 2 diabetes. Nature 2006;444:840–846.
2. Hales CM, Carroll MD, Fryar CD, et al. Prevalence of obesity among adults and youth: United States, 2015–2016. NCHS Data Brief 2017:1–8.
3. Benedict M, Zhang X. Non-alcoholic fatty liver disease: aAn expanded review. World J Hepatol 2017;9:715–732.
4. Cotter TG, Rinella M. Nonalcoholic fatty liver disease 2020: the state of the disease. Gastroenterology 2020; 158:1851–1864.
5. Ringelhan M, Pfister D, O'Connor T, et al. The immunology of hepatocellular carcinoma. Nat Immunol 2018; 19:222–232.
6. Font-Burgada J, Sun B, Karin M. Obesity and cancer: the oil that feeds the flame. Cell Metab 2016;23:48–62.
7. Portillo Sanchez P, Bril F, Maximos M, et al. High prevalence of nonalcoholic fatty liver disease in patients with type 2 diabetes mellitus and normal plasma aminotransferase levels. J Clin Endocrinol Metab 2014; 100:2231–2238.
8. Sanyal AJ, Campbell-Sargent C, Mirshahi F, et al. Nonalcoholic steatohepatitis: association of insulin resistance and mitochondrial abnormalities. Gastroenterology 2001;120:1183–1192.
9. Morgantini C, Jager J, Li XD, et al. Liver macrophages regulate systemic metabolism through non-inflammatory factors. Nat Metab 2019;1:445–459.
10. Trefts E, Gannon M, Wasserman DH. The liver. Curr Biol 2017;27:R1147–R1151.

11. Degli Esposti D, Hamelin J, Bosselut N, et al. Mitochondrial roles and cytoprotection in chronic liver injury. Biochem Res Int 2012;2012:387626.
12. Balaban RS, Nemoto S, Finkel T. Mitochondria, oxidants, and aging. Cell 2005;120:483–495.
13. Starkov AA. The role of mitochondria in reactive oxygen species metabolism and signaling. Ann N Y Acad Sci 2008;1147:37–52.
14. Murphy MP. How mitochondria produce reactive oxygen species. Biochem J 2009;417:1–13.
15. Mansouri A, Gattolliat CH, Asselah T. Mitochondrial dysfunction and signaling in chronic liver diseases. Gastroenterology 2018;155:629–647.
16. Pessayre D, Fromenty B. NASH: a mitochondrial disease. J Hepatol 2005;42:928–940.
17. Perez-Carreras M, Del Hoyo P, Martin MA, et al. Defective hepatic mitochondrial respiratory chain in patients with nonalcoholic steatohepatitis. Hepatology 2003; 38:999–1007.
18. Bartel DP. MicroRNAs: Genomics, biogenesis, mechanism, and function. Cell 2004;116:281–297.
19. Bartel DP. MicroRNAs: Target recognition and regulatory functions. Cell 2009;136:215–233.
20. Sripada L, Tomar D, Singh R. Mitochondria: one of the destinations of miRNAs. Mitochondrion 2012;12:593–599.
21. Li PF, Jiao JQ, Gao GF, et al. Control of mitochondrial activity by miRNAs. J Cell Biochem 2012;113:1104–1110.
22. Azzimato V, Jager J, Chen P, et al. Liver macrophages inhibit the endogenous antioxidant response in obesity-associated insulin resistance. Sci Transl Med 2020;12: eaaw9709.
23. Huang HC, Nguyen T, Pickett CB. Phosphorylation of Nrf2 at Ser-40 by protein kinase C regulates antioxidant response element-mediated transcription. J Biol Chem 2002;277:42769–42774.
24. Pi J, Bai Y, Reece JM, et al. Molecular mechanism of human Nrf2 activation and degradation: role of sequential phosphorylation by protein kinase CK2. Free Radic Biol Med 2007;42:1797–1806.
25. Jain AK, Jaiswal AK. GSK-3beta acts upstream of Fyn kinase in regulation of nuclear export and degradation of NF-E2 related factor 2. J Biol Chem 2007;282:16502–16510.
26. Taguchi K, Motohashi H, Yamamoto M. Molecular mechanisms of the Keap1-Nrf2 pathway in stress response and cancer evolution. Genes Cells 2011; 16:123–140.
27. Joo MS, Kim WD, Lee KY, et al. AMPK facilitates nuclear accumulation of Nrf2 by phosphorylating at Serine 550. Mol Cell Biol 2016;36:1931–1942.
28. Sarcinelli C, Dragic H, Piecyk M, et al. ATF4-dependent NRF2 transcriptional regulation promotes antioxidant protection during endoplasmic reticulum stress. Cancers (Basel) 2020;12:569.
29. Mitsuishi Y, Taguchi K, Kawatani Y, et al. Nrf2 redirects glucose and glutamine into anabolic pathways in metabolic reprogramming. Cancer Cell 2012;22:66–79.
30. Holmstrom KM, Baird L, Zhang Y, et al. Nrf2 impacts cellular bioenergetics by controlling substrate availability for mitochondrial respiration. Biol Open 2013;2:761–770.
31. Linker RA, Lee DH, Ryan S, et al. Fumaric acid esters exert neuroprotective effects in neuroinflammation via activation of the Nrf2 antioxidant pathway. Brain 2011; 134:678–692.
32. Kinch L, Grishin NV, Brugarolas J. Succination of Keap1 and activation of Nrf2-dependent antioxidant pathways in FH-deficient papillary renal cell carcinoma type 2. Cancer Cell 2011;20:418–420.
33. Ashrafian H, Czibik G, Bellahcene M, et al. Fumarate is cardioprotective via activation of the Nrf2 antioxidant pathway. Cell Metab 2012;15:361–371.
34. Mills EL, Ryan DG, Prag HA, et al. Itaconate is an anti-inflammatory metabolite that activates Nrf2 via alkylation of KEAP1. Nature 2018;556:113.
35. Aouadi M, Tesz GJ, Nicoloro SM, et al. Orally delivered siRNA targeting macrophage Map4k4 suppresses systemic inflammation. Nature 2009;458:1180–1184.
36. Aparicio-Vergara M, Tencerova M, Morgantini C, et al. Isolation of Kupffer cells and hepatocytes from a single mouse liver. Methods Mol Biol 2017;1639:161–171.
37. Rosner B. Fundamentals of biostatistics. Boston: Brooks/Cole, Cengage Learning, 2011.
38. Lampropoulou V, Sergushichev A, Bambouskova M, et al. Itaconate links inhibition of succinate dehydrogenase with macrophage metabolic remodeling and regulation of inflammation. Cell Metab 2016;24:158–166.
39. Cassim S, Raymond VA, Lapierre P, et al. From in vivo to in vitro: major metabolic alterations take place in hepatocytes during and following isolation. PLoS One 2017; 12:e01190366.
40. Williams NC, O'Neill LAJ. A role for the Krebs cycle intermediate citrate in metabolic reprogramming in innate immunity and inflammation. Front Immunol 2018;9:141.
41. Li X, Higashida K, Kawamura T, et al. Alternate-day high-fat diet induces an increase in mitochondrial enzyme activities and protein content in rat skeletal muscle. Nutrients 2016;8:203.
42. Messa GAM, Piasecki M, Hurst J, et al. The impact of a high-fat diet in mice is dependent on duration and age, and differs between muscles. J Exp Biol 2020;223: jeb217117.
43. Mills EL, Kelly B, Logan A, et al. Succinate dehydrogenase supports metabolic repurposing of mitochondria to drive inflammatory macrophages. Cell 2016;167:457–470.e13.
44. Meiser J, Kramer L, Sapcariu SC, et al. Pro-inflammatory macrophages sustain pyruvate oxidation through pyruvate dehydrogenase for the synthesis of itaconate and to enable cytokine expression. J Biol Chem 2016; 291:3932–3946.
45. Cordes T, Wallace M, Michelucci A, et al. Immunoresponsive gene 1 and itaconate inhibit succinate dehydrogenase to modulate intracellular succinate levels. J Biol Chem 2016;291:14274–14284.

46. Bambouskova M, Gorvel L, Lampropoulou V, et al. Electrophilic properties of itaconate and derivatives regulate the IkappaBzeta-ATF3 inflammatory axis. Nature 2018;556:501–504.
47. Michelucci A, Cordes T, Ghelfi J, et al. Immune-responsive gene 1 protein links metabolism to immunity by catalyzing itaconic acid production. Proc Natl Acad Sci U S A 2013;110:7820–7825.
48. Hiller K, Michelucci A, Cordes T, et al. Method to predict the presence of inflammation or itaconic acid, irg1 and/or protein irg1 in a subject and pharmaceutical composition for treating or preventing inflammation. Patent Number: WO2013041692. Available at: https://patentscope.wipo.int/search/en/detail.jsf?docId=WO2013041692. Published March 28, 2013.
49. Swain A, Bambouskova M, Kim H, et al. Comparative evaluation of itaconate and its derivatives reveals divergent inflammasome and type I interferon regulation in macrophages. Nat Metab 2020;2:594–602.
50. Deschauer M, Gizatullina Z, Schulze A, et al. Molecular and biochemical investigations in fumarase deficiency. Mol Genet Metab 2006;88:146–152.
51. Perks KL, Ferreira N, Richman TR, et al. Adult-onset obesity is triggered by impaired mitochondrial gene expression. Science Advances 2017;3.
52. Putti R, Sica R, Migliaccio V, et al. Diet impact on mitochondrial bioenergetics and dynamics. Front Physiol 2015;6:109.
53. Anderson EJ, Lustig ME, Boyle KE, et al. Mitochondrial H2O2 emission and cellular redox state link excess fat intake to insulin resistance in both rodents and humans. Journal of Clinical Investigation 2009;119:573–581.
54. Zorzano A, Liesa M, Palacin M. Role of mitochondrial dynamics proteins in the pathophysiology of obesity and type 2 diabetes. Int J Biochem Cell Biol 2009;41:1846–1854.
55. Runtsch MC, O'Neill L. Itaconate inhibits alternative activation of macrophages by targeting Janus Kinase 1. J Immunol 2019:202.
56. O'Neill LAJ, Artyomov MN. Itaconate: the poster child of metabolic reprogramming in macrophage function. Nat Rev Immunol 2019;19:273–281.
57. Kelly B, O'Neill LAJ. Metabolic reprogramming in macrophages and dendritic cells in innate immunity. Cell Res 2015;25:771–784.
58. Galvan-Pena S, O'Neill LA. Metabolic reprograming in macrophage polarization. Front Immunol 2014;5:420.
59. Weaver TM, Levitt DG, Donnelly MI, et al. The multisubunit active-site of fumarase-C from *Escherichia-Coli*. Nature Structural Biology 1995;2:654–662.
60. Hooftman A, Angiari S, Hester S, et al. The immunomodulatory metabolite itaconate modifies NLRP3 and inhibits inflammasome activation. Cell Metab 2020;32:468–489.e7.
61. Jha AK, Huang SCC, Sergushichev A, et al. Network integration of parallel metabolic and transcriptional data reveals metabolic modules that regulate macrophage polarization. Immunity 2015;42:419–430.
62. Yang H, Wu JW, Wang SP, et al. Adipose-specific deficiency of fumarate hydratase in mice protects against obesity, hepatic steatosis, and insulin resistance. Diabetes 2016;65:3396–3409.
63. Cullinan SB, Gordan JD, Jin JO, et al. The Keap1-BTB protein is an adaptor that bridges Nrf2 to a Cul3-based E3 ligase: oxidative stress sensing by a Cul3-Keap1 ligase. Mol Cell Biol 2004;24:8477–8486.
64. Taguchi K, Motohashi H, Yamamoto M. Molecular mechanisms of the Keap1-Nrf2 pathway in stress response and cancer evolution. Genes to Cells 2011;16:123–140.
65. Vomund S, Schafer A, Parnham MJ, et al. Nrf2, the master regulator of anti-oxidative responses. Int J Mol Sci 2017;18:2772.
66. Edwards CB, Copes N, Brito AG, et al. Malate and fumarate extend lifespan in *Caenorhabditis elegans*. PLoS One 2013;8:e58345.
67. Hammer A, Waschbisch A, Kuhbandner K, et al. The NRF2 pathway as potential biomarker for dimethyl fumarate treatment in multiple sclerosis. Ann Clin Transl Neurol 2018;5:668–676.
68. Lin YJ, Lin IC, Yu HR, et al. Early postweaning treatment with dimethyl fumarate prevents prenatal dexamethasone- and postnatal high-fat diet-induced programmed hypertension in male rat offspring. Oxid Med Cell Longev 2018;2018:5343462.
69. Krzystanek E, Jarosz-Chobot P. Dimethyl fumarate in a patient with multiple sclerosis and type 1 diabetes mellitus: the importance of ketonuria. Mult Scler Relat Disord 2018;21:42–45.
70. Li Y, Ma FZ, Li HM, et al. Dimethyl fumarate accelerates wound healing under diabetic conditions. J Mol Endocrinol 2018;61:163–172.
71. Satoh T, Lipton S. Recent advances in understanding NRF2 as a druggable target: development of pro-electrophilic and non-covalent NRF2 activators to overcome systemic side effects of electrophilic drugs like dimethyl fumarate. F1000Res 2017;6:2138.

Received August 18, 2020. Accepted August 15, 2021.

Correspondence
Address correspondence to: Myriam Aouadi, PhD, and Valerio Azzimato, PhD, Center for Infectious Medicine (CIM), Department of Medicine, Karolinska Institutet, ANA Futura, Alfred Nobels allé 8, 141 52 Huddinge, Sweden. e-mail: myriam.aouadi@ki.se; valerio.azzimato@ki.se.

CRediT Authorship Contributions
Valerio Azzimato, PhD (Conceptualization: Lead; Data curation: Lead; Formal analysis: Lead; Investigation: Lead; Methodology: Lead; Project administration: Equal; Validation: Lead; Visualization: Lead; Writing – original draft: Lead). Ping Chen, PhD (Data curation: Supporting; Investigation: Supporting; Methodology: Supporting; Visualization: Supporting; Writing - original: Supporting; Validation: Supporting). Emelie Barreby, MSc (Data curation: Supporting; Investigation: Supporting; Methodology: Supporting; Resources: Supporting; Validation: Supporting). Cecilia Morgantini, MD, PhD (Data curation: Supporting; Investigation: Supporting; Methodology: Supporting; Resources: Supporting; Validation: Supporting). Laura Levi, PhD (Data curation: Supporting; Investigation: Supporting; Methodology: Supporting; Resources: Supporting; Validation: Supporting). Ana Vankova, MSc (Data curation: Supporting; Investigation: Supporting; Methodology: Supporting). Jennifer Jager, PhD (Data curation: Supporting; Investigation: Supporting; Methodology: Supporting), André Sulen, PhD (Data curation: Supporting; Investigation: Supporting; Methodology: Supporting), Marina Diotallevi, PhD (Data curation: Supporting; Investigation: Supporting; Methodology: Supporting). Joanne X. Shen, PhD (Investigation: Supporting; Methodology: Supporting), Anne Miller, PhD (Data curation: Supporting; Investigation: Supporting; Methodology: Supporting). Ewa Ellis, PhD

(Resources: Supporting). Mikael Rydén, MD, PhD (Resources: Supporting). Erik Näslund, MD (Resources: Supporting). Anders Thorell, PhD (Resources: Supporting). Volker M. Lauschke, PhD (Resources: Supporting; Methodology: Supporting). Keith M. Channon, FRCP, FMedSci (Resources: Supporting; Methodology: Supporting). Mark J. Crabtree, PhD (Resources: Supporting; Methodology: Supporting). Arvand Haschemi, PhD (Resources: Supporting; Methodology: Supporting; Visualization: Supporting). Siobhan M. Craige, PhD (Investigation: Supporting; Formal analysis: Supporting; Visualization: Supporting; Writing – original draft: Supporting). Mattia Mori, PhD (Resources: Supporting; Methodology: Supporting; Investigation: Supporting; Formal analysis: Supporting; Visualization: Supporting; Writing – original draft: Supporting). Francesco Spallotta, PhD (Resources: Supporting; Methodology: Supporting; Investigation: Supporting; Formal analysis: Supporting; Visualization: Supporting; Writing – original draft: Supporting). Myriam Aouadi, PhD (Conceptualization: Lead; Data curation: Equal; Formal analysis: Equal; Funding acquisition: Lead; Investigation: Lead; Methodology: Equal; Project administration: Lead; Resources: Lead; Supervision: Lead; Writing – original draft: Lead)

Conflict of interest
This author discloses the following: Volker M. Lauschke is founder, CEO, and shareholder of HepaPredict AB, and performs consultancy work for EnginZyme AB. The remaining authors disclose no conflicts.

Funding
This project has received funding from the European Research Council (ERC) under the European Union's Horizon 2020 research and innovation program (Myriam Aouadi: grant agreement no. 864788; Mikael Rydèn: ERCSyG no. 856404), the Swedish Research Council (Volker M. Lauschke: 2016-01153 and 2016-01154; Myriam Aouadi: 2019-01837, 2019-01056, and 2015-0358), the Novo Nordisk Foundation, including the Tripartite and Meriad Immunometabolism Consortium (Myriam Aouadi, Keith M. Channon, and Mikael Rydèn: NNF15CC0018486 and NNF 0064142; Myriam Aouadi: NNF19OC0057127 and NNF19OC0059200), the EFSD supported by EFSD/Lilly European Diabetes Research Program (Myriam Aouadi: 97026), by the EU/EFPIA/OICR/McGill/KTH/Diamond Innovative Medicines Initiative 2 Joint Undertaking (Volker M. Lauschke: EUbOPEN grant no. 875510), the Erling-Persson Family Foundation (Anders Thorell: FEPS-2019-0200), the AIRC, Associazione Italiana per la Ricerca sul Cancro, My First AIRC Grant, (Francesco Spallotta: ID number 23099), the Strategic Research Programs in Regenerative Medicine (Volker M. Lauschke) and Diabetes (Volker M. Lauscke and Myriam Aouadi) at Karolinska Institutet and the Karolinska Institutet (Valerio Azzimato: grant no. 2020-02019; Myriam Aouadi: grant no. 2-2111/2019).

Transcript profiling
GSE132795, GSE132800, and GSE132801.

Supplementary Experimental Procedures

Human Subjects

Liver samples were obtained from a total of 15 individuals, including 10 obese patients (body mass index between 34.7 and 40.8 kg/m^2) undergoing laparoscopic Roux-en-Y gastric bypass surgery at Danderyd Hospital or Ersta Hospital in Stockholm, Sweden. Liver cells were obtained from 5 nonobese patients and isolated by the Liver Cell Laboratory at the Unit of Transplantation Surgery, Department of Clinical Science, Intervention and Technology (CLINTEC) at Karolinska Institutet, Sweden. None of the participants had any previous history of cardiovascular disease, diabetes, gastrointestinal disease, systemic illness, alcohol abuse, coagulopathy, chronic inflammatory disease, any clinical sign of liver damage, or surgical intervention within 6 months before the study. Patients did not follow any special diet before the surgery. Insulin sensitivity was assessed by homeostatic model assessment (HOMA-IR).[1] Of the obese patients, 5 patients with HOMA-IR <2 were defined as obese insulin-sensitive and 5 with HOMA-IR >4 as obese insulin-resistant. Hepatic steatosis index was calculated as in Lee et al.[2] The Regional Ethical Committee in Stockholm approved the study and all the subjects gave written informed consent for all procedures before their participation. Liver cells from nonobese patients were obtained from liver donors and isolated by the Liver Cell Laboratory at the Unit of Transplantation Surgery, CLINTEC at Karolinska Institutet. Full metabolic parameters of the obese human cohort used in the study have been published in Azzimato et al.[3] and are stated in Supplementary Table 1.

Cell Cultures and Treatments

Murine-derived macrophage RAW 264.7 cells were cultured in RPMI 1640 medium (Sigma-Aldrich, St. Louis, MO) supplemented with 10% fetal bovine serum (FBS), 1% penicillin/streptomycin (Life Technologies, Carlsbad, CA), and 1% L-glutamine (Sigma-Aldrich) at 37 °C, 95% humidity, and 5% CO_2. Human monocyte-like THP-1 cells (American Type Culture Collection, Manassas, VA) were grown in RPMI 1640 medium (Sigma-Aldrich) supplemented with 10% FBS, 1% penicillin/streptomycin (Life Technologies), and L-glutamine (Sigma-Aldrich) at 37 °C, 95% humidity, and 5% CO_2. Before performing the experiments, THP-1 cells were incubated with PMA for 24 hours and were allowed to differentiate into macrophages. Cells were stimulated with LPS at different concentrations (10 ng/mL or 100 ng/mL) for 6 hours and/or with 100 μM of 4-OI (Sigma-Aldrich; SML2338) and then processed for additional experiments.

antagomiR and Mimic Transfections

THP-1 cells were mixed with a pre-incubated mixture of Lipofectamine RNAiMAX (Invitrogen, Carlsbad, CA) and amiR/inhibitor or mimic constructs (amiR-144, scr, and mimic-miR-144) (1 nmol amiR or mimic/inhibitor per 300,000 cells) in OptiMEM (Gibco, Waltham, MA). Cells were harvested after 24 hours of treatment for downstream experiments.

Mice and Diet

Four-week-old wild-type C57BL/6J (WT) and 5-week-old *ob/ob* male mice were obtained from Charles River Laboratories International, Inc. (Wilmington, MA) and maintained on a 12-hour light/dark cycle. Animals were given free access to food and water. C57BL/6J WT mice were fed an HFD composed of 60% calories from fat, 20% from carbohydrates, 20% from protein (Research Diets Inc., New Brunswick, NJ) at 5 weeks of age. Control mice were fed a normal chow diet. All experiments were performed at 9 weeks for HFD mice, or at 9 and 14 weeks for *ob/ob* mice. All procedures were performed in accordance with guidelines approved by the Ethical Committee (Linköpings djurförsöksetiska nämnd).

GeRP Administration by Intravenous Injection In Vivo

GeRPs were prepared as previously described.[4] WT mice fed an HFD for 7 weeks were randomized to groups according to their body weight and glucose tolerance. Mice were then treated with 12.5 mg/kg GeRPs loaded with miRIDIAN microRNA mmu-miR-144–5p hairpin inhibitor (GeRP-amiR-144) (Dharmacon, Lafayette, CO) and Endoporter (2.27 mg/kg) or with miRIDIAN microRNA hairpin inhibitor negative control #1 (Dharmacon) (247 μg/kg) and Endoporter (2.27 mg/kg) as a nontargeting scrambled control. Mice received 6 doses of fluorescently labeled GeRPs by intravenous injection over 15 days.

Isolation of LMs and Hepatocytes From Mice

LMs and hepatocytes were isolated as previously described.[5] Briefly, livers of anesthetized mice were first perfused with calcium-free Hanks' balanced salt solution (HBSS), followed by collagenase digestion. After digestion, the hepatocytes were released by mechanical dissociation of the lobes and underwent several steps of filtration with calcium-containing HBSS and centrifugation at 50*g* for 3 minutes. The resulting hepatocyte pellet was washed twice and plated. The supernatant containing non-parenchymal cells was loaded on a Percoll gradient (25% and 50%) and centrifuged for 30 minutes at 1155 g and 4°C. The interphase ring with enriched LMs was collected. The cells were then plated for 30 minutes and washed twice before RNA or proteins were extracted for subsequent analyses.

Isolation of LMs From Humans and 4-Octyl Itaconate Treatment

Human liver samples used for isolation of NPCs were collected from patients undergoing liver resection surgery for primary or secondary liver malignancies, where only nontumor tissue was used. In brief, the livers were subjected to a series of flushing steps to remove excess blood. Thereafter, livers were digested by perfusion with Collagenase XI (Sigma-Aldrich) and NPCs were isolated by

several centrifugation steps. Finally, cells were cryopreserved in FBS with 10% dimethyl sulfoxide and stored in liquid nitrogen until further use. The supernatant containing NPCs were loaded on a Percoll gradient and LMs isolated as described previously. Human LMs were plated in presence of 240 μM oleic acid (Sigma-Aldrich) and 240 μM palmitic acid (Sigma-Aldrich) for 24 hours. Human LMs were then treated with 100 μM 4-OI (Sigma-Aldrich) and then processed for additional experiments

Reactive Oxygen Species Content Measurement

Intracellular ROS were determined using DCFDA / H2DCFDA - Cellular ROS Assay Kit (Abcam, Cambridge, UK; ab113851) following the manufacturer's instructions.

Intracellular Itaconate Measurement

Itaconate levels were measured using high-performance liquid chromatography (HPLC). Cell pellets were resuspended in PBS and lysed by freeze-thaw cycles. Cell debris was removed by centrifugation at 17,000*g* for 10 minutes at 4°C and a small volume of debris-free lysate was kept for protein concentration analysis; 10% of 2M perchloric acid was then added to the lysates to precipitate proteins that were removed by second centrifugation.

Once cleared, lysates were injected onto a column of 250 mm, ACE C-18 column (Hichrom, Reading, UK) and itaconate was detected using a UV lamp set at 210 nm. HPLC separation was performed using a mobile phase made of 2.5% acetonitrile and 0.1% phosphoric acid (all ultrapure electrochemical HPLC grade), at a flow rate of 1.0 mL/min. Quantification of itaconate in samples was made by comparison with standard itaconate (Sigma-Aldrich; I29204) ranging from 10 pmol to 50,000 pmol. Results were normalized using the protein concentration of each sample.

Metabolic Assays and In Situ Single-Cell Activity Assays

Succinate dehydrogenase activity was measured using Succinate Dehydrogenase Activity Assay Kit (Colorimetric) (Abcam; ab228560). Fumarate hydratase activity was measured using Fumarase Activity Assay Kit (Colorimetric) (Abcam; ab196992). Succinate intracellular levels were measured using Succinate Assay Kit (Colorimetric) (Abcam; ab204718). Fumarate intracellular levels were measured using Fumarate Assay Kit (Colorimetric) (Abcam; ab102516). All assays were performed following the manufacturer's instructions. In situ single-cell enzyme activity assays for SDH, lactate dehydrogenase (LDH), isocitrate dehydrogenase 3 (IDH3), and glucose-6-phosphate dehydrogenase (G6PDH) were performed as previously described.[6] Briefly, consecutive nonfixed cryo-sections of mouse liver tissues were assayed for 15 minutes by established enzyme histochemistry protocols[7] and incubated with 4′,6-diamidino-2-phenylindole (DAPI) for subsequent nuclear cell segmentation and identification (fluorescein isothiocyanate + GeRP targeted cells) in whole-mount tissue scan analysis (TissueFAXS). Mean enzyme activity values (staining intensities) given per cell were compared between the groups.

Isolation of RNA, microRNA, Real-Time Quantitative PCR, and RNA Library Preparation

Total RNA and microRNA extraction and purification were performed using the TRIzol Reagent (ThermoFisher Scientific) or the miRNeasy mini kit (Qiagen, Hilden, Germany) following the manufacturers' protocol. For miRNA analysis, 100 ng total RNA were reverse-transcribed and amplified in real-time polymerase chain reaction (PCR) using miScript-System including miScript RT-Kit (Qiagen), miScript SYBR-Green PCR-Kit, and miScript Primer Assay miRBase v12 (Qiagen) according to the manufacturer's protocol. Specific primers for hsa-miR-144 (Qiagen) and mmu-miR-144 were used for stem-loop qPCR. For internal control the expression of the small nuclear RNAs RNU6B (Qiagen) was determined. For real-time quantitative PCR (qPCR), complementary DNA (cDNA) was synthesized from 0.5 μg of total RNA using iScript cDNA Synthesis Kit (Bio-Rad, Hercules, CA) according to the manufacturer's instructions. Synthesized cDNA forward and reverse primers along with the Sso Advanced Universal SYBR-Green Supermix were run on the CFX96 Real-time PCR System (Bio-Rad); 60S acidic ribosomal protein P0 (rplp0) or b-actin were used as reference genes in mice and humans. Primer sequences used for qPCR: mouse *Irg1* (FW: 5′- GCAACATGATGCTCAAGTCTG-3′; REV: 5′- TGCTCCTCCGAATGATACCA-3′), mouse *Tnf-α* (FW: 5′-CCCTCACACTCAGATCATCTTCT-3′; REV: 5′-GCTACGACGTGGGCTACAG-3′), mouse *β*-actin (FW: 5′-TCTACAATGAGCTGCGTGTGG-3′; REV: 5′-GTACATGGCTGGGGTGTTGAA-3′), human *IRG1* (FW: 5′-AGAAGCCCTGCCAAGGAGTCCAAA-3′; REV: 5′- CCAGAGCTTCTCGGCACTTTGTCG-3′), human *TNF-α* (FW: 5′-ATGAGCACTGAAAGCATGATCC-3′; REV: 5′-GAGGGCTGATTAGAGAGAGGTC-3′), human NRF2 (FW: 5′-CAGCGACGGAAAGAGTATGA- 3′; REV: 5′-TGGGCAACCTGG GAGTAG-3′), human NQO1 (FW: 5′- GGCAGAAGAGCACTGATCGTA-3′; REV:5′-TGATGGGA TTGAAGTTCATGGC-3′), human GSTP1 (FW: 5′-GTAGTTTGCCCAAGGTCAAG-3′; REV: 5′- AGCCACCTGAGGGGTAAG-3′), human CES2G (FW: 5′-GTCTTCGCTTGTTGTGTCC-3′; REV: 5′- CGAAGGAGAAAGGCAATGAC-3′), human *HMOX1* (FW: 5′-CACGCATATACCCGCTACCT-3′; REV: 5′-CCAGAGTGTTCATTCGAGCA-3′), human *RPLP0* (FW: 5′-CAGATTGGCTACCCAACTGTT-3′; REV: 5′- GGGAAGGTGTAATCCGTCTCC-3′).

For library preparation, RNA integrity was determined using an Agilent (Santa Clara, CA) Bioanalyzer. Libraries from mouse RNA were prepared using TruSeq Stranded mRNA kit (Illumina, San Diego, CA). The concentration of indexed libraries was quantified by reverse-transcription (RT)-qPCR using the Universal Kapa Library Quantification Kit (KAPA Biosystems, Wilmington, MA). Final libraries were normalized and sequenced on an Illumina HiSeq 3000 sequencer.

Nuclei and Library Preparation for Global Run-On Sequencing

Global run-on sequencing (GRO-seq) was performed as previously described,[8] with minor modifications for mouse liver macrophage samples. Nuclei were extracted from liver macrophages (3–4 pooled mice/group) using hypotonic buffer, and visually inspected for quality under a microscope with DAPI staining. The total number of nuclei was determined using a Countess Automated Cell Counter (Bio-Rad). Nuclear run-on was performed using Br-UTP followed by enrichment with anti-Br-UTP antibodies, reverse transcription, and library preparation.

Molecular Dynamics Simulations

The full-length homo-dimeric human FH coded by PDB ID: 3E04 was used as the reference structure in this computational study. Missing gaps were filled by homology modeling with the Prime software,[9] using the crystallographic structure of FH coded by PDB ID 5UPP[10] as a structural template. MD simulations were carried out with Amber18 (University of California).[11] The ff14SB force field was used for the protein, and the general amber force field was used for organic molecules. The protonation state of histidine residues in monomeric FH was assigned by the H++ server (http://biophysics.cs.vt.edu)[12] and refined by visual inspection in the homo-tetrameric form of the enzyme. The itaconate protonation state was assigned by QUACPAC (OpenEye Scientific Software, Santa Fe, NM; http://www.eyesopen.com), and formal charges were computed at the am1-bcc level of theory. The system was prepared by placing 4 itaconate molecules at random positions around tetrameric FH, at a distance higher than 20 Å. Then, TIP3P-type water molecules and Na^+ counterions were added to the simulation box buffering 10 Å from the molecular system to solvate the solute and to neutralize the total charge, respectively. Then, the whole system was relaxed by adapting a MD protocol previously described,[13–16] which consists of (1) energy minimization of the solvent (4000 steps); (2) energy minimization of the solvated solute (5000 steps); (3) heating from 0 to 300 K at constant volume (1 ns); (4) density equilibration at constant pressure (1 ns); (5) system equilibration at constant pressure (50 ns); and (6) MD trajectory production at constant pressure (500 ns). The MD trajectory was analyzed by the cpptraj software,[17] and theoretical affinity was computed by the MMPBSA.py program within the frames that correspond to the most populated cluster of MD frames.[18]

Liver Spheroids

antagomiR transfections. Cryopreserved primary human hepatocytes (Heps) (Bioreclamation IVT, Westbury, NY) were mixed with a pre-incubated mixture of Lipofectamine RNAiMAX (Invitrogen) and amiR/inhibitor constructs (1 nmol amiR/inhibitor per 300,000 cells) in OptiMEM (Gibco). In the case of co-culture transfections, cryopreserved hepatocytes and isogenic non-parenchymal cells (NPCs) (Bioreclamation IVT) were transfected separately in suspension with a pre-incubated mixture of Lipofectamine RNAiMAX and amiR/inhibitor constructs (1 nmol amiR/inhibitor per 300,000 cells) in OptiMEM. Cells were transfected for 5 hours with occasional agitation of the suspension. All transfections were performed using low glucose/insulin medium (PAN-Biotech, supplemented with 5.5 mM D-glucose, 0.1 nM insulin, 2 mM L-glutamine, 100 units/mL penicillin, 100 μg/mL streptomycin, 5.5 μg/mL transferrin, 6.7 ng/mL sodium selenite, 100 nM dexamethasone, and 10% FBS).

Spheroid formation. Spheroids were formed from hepatocytes monocultures or from co-cultures of hepatocytes and NPCs as indicated. In the case of co-cultures, separately transfected hepatocytes and NPCs were seeded at a ratio of 3:1 (Heps:NPCs). Cells were seeded in ultra-low attachment 96-well plates (Corning, Corning, NY) as previously described[19] and were cultured in low glucose/insulin medium. Following seeding, plates were centrifuged at 180*g* for 2 minutes. After 6 days, when the spheroids were sufficiently compact, 50% of the medium was exchanged for serum-free culture medium.

FFA supplementation. FFAs were conjugated to 10% bovine serum albumin (Sigma-Aldrich) at a molar ratio of 1:5 for 2 hours at 40 °C. Spheroids were treated with 240 μM oleic acid (Sigma-Aldrich) and 240 μM palmitic acid (Sigma-Aldrich) in serum-free high glucose/insulin medium (Gibco) supplemented with 11.1 mM D-glucose, 1.7 μM insulin, 2 mM L-glutamine, 100 units/mL penicillin, 100 μg/mL streptomycin, 5.5 μg/mL transferrin, 6.7 ng/mL sodium selenite, and 100 nM dexamethasone for 5 days. Untreated spheroids were maintained in serum-free low glucose/insulin medium. All treatments were performed 8 days after seeding once spheroids were aggregated.

Western Blot and Immunoprecipitation Assay

An amount of 30 μg of proteins were fractionated by sodium dodecyl sulfate–polyacrylamide gel electrophoresis using precast 4% to 12% gradient gels (ThermoFisher Scientific), transferred to polyvinylidene difluoride membranes (ThermoFisher Scientific) and probed with an appropriate dilution of the primary antibodies indicated as follows. This was followed by incubation with the appropriate horseradish peroxidase–conjugated secondary antibody (Abcam; ab6721 or ab6789). Finally, bound secondary antibodies were visualized by ECL detection reagent (Bio-Rad) and images were acquired by an imaging system equipped with charge-coupled device camera (ChemiDoc, Bio-Rad). Immunoprecipitations for KEAP1 (Santa Cruz Biotechnology, Dallas, TX; sc-514914) were performed on 1000 μg of proteins. Lysates were incubated overnight with Agarose Protein G plus mixture (Pierce, Rockford, IL) and protein complexes were eluted in Laemmli buffer. Then, Western Blot analysis was performed as described previously. The following primary antibodies were used: IRG1 (Abcam; ab222411), KEAP1 (Santa Cruz Biotechnology; sc-514914), CUL-3 (Santa Cruz Biotechnology; sc-166110); NRF2 (phospho S40) (Abcam; 76026), and β-actin (Abcam; ab179467).

Bioinformatics

In silico analysis of mir-144 predicted targets. Mouse miR-144–5p predicted targets were retrieved from miRWalk 2.0[20] holistic view files. Target genes selected for overrepresentation analysis were based on following criteria: they were (1) significantly downregulated in *ob/ob* mice compared with WT mice, (2) predicted as targets by at least 2 of 13 different miRNA-gene prediction algorithms, and (3) predicted targets at both 9 and 14 weeks.

Retrieving raw sequencing data. Signal intensities were converted to individual base calls during the sequence run using the system's real-time analysis software. Sample de-multiplexing and conversion to fastq-files was performed using Illumina's bcl2fastq software with all default options. The distribution of reads per sample in a lane was within reasonable tolerance.

mRNA-seq alignment and gene quantification for HFD and ND mice. Raw fastq-files (PRJNA483744)[21] were aligned against the murine genome version mm10 using TopHat version v2.0.13[22] with all default options. BAM files containing the alignment results were sorted according to the mapping position. mRNA quantification was performed using FeatureCounts from the Subread package[23] against the GRCm38-gencode transcripts database version 7 (gencode.vM7.annotation.gtf) and the GRCh38-genocode transcripts database version 24 (gencode.v24.annotation.gtf) to obtain read counts for each individual Ensembl gene.

GRO-seq data processing and gene quantification for HFD and ND mice. Raw fastq-files (PRJNA483744)[21] were aligned against the murine genome version mm10 using BWA[22] with samse option. Uniquely mapped reads were extended to 150 base pairs in the 5′ to 3′ direction and used for downstream analysis. Nascent transcription of genes was measured using GRO-seq reads mapped to the sense strand of the gene in a 10-kb window (+2 kb to +12 kb relative to transcription start site) within the gene symbol annotated gene body. Smaller genes between 2 kb and 12 kb in length were quantified using smaller window size, from +2 kb to the transcription end site. For genes shorter than 2 kb, the entire gene body was used for the quantification. The mapped reads within each gene quantification window were counted using bedtools with the intersect option[24] and expressed as reads per kilobase per million reads (RPKM). Genes with transcription levels greater than 0.3 RPKM were considered as being actively transcribed. Genes that were not transcribed throughout all conditions were eliminated before downstream analysis. A gene was defined as "differential" between a given pair of conditions if it was transcribed in either condition and the fold change was greater than 1.5 (either up or down).

Analysis of RNA sequencing data from ob/ob and WT mice. Raw reads were aligned to the mouse genome mm10 (genome build GRCm38.p5) using STAR aligner[25] and followed by expression quantification at gene level based on Gencode M14 annotation using the Cufflinks pipeline.[26] Cuffdiff[27] was used to identify genes differentially expressed between *ob/ob* and WT mice. GO enrichment and pathway overrepresentation analysis were further performed on differentially expressed genes between conditions (adjusted P value $< .05$ and log2-scale fold change > 1 or < -1). Raw fastq-files and processed data are available in GEO repository (GSE132801, GSE132800).

Analysis of small RNA-seq data. After removing the adaptors from the raw reads by Cutadapt,[28] ShortStack[29] was used to align the small RNA reads against GENCODE mouse primary assembly (release M14, GRCm38.p5) and further identify the miRNA clusters in de novo mode. ShortStack quantified the expression of the most abundant RNAs (MajorRNA) at locus as reads per million (RPM) but ignored the quantification for less abundant RNAs (MinorRNA) at the same locus. This could result in false negative discovery of certain miRNAs that are truly expressed in the samples but show no expression due to the quantification. Here, post-processing was performed to quantify the less abundant RNAs by retrieving read counts from the MinorRNA alignments and converted into RPMs. All quantified miRNAs were then annotated into miRBase by aligning the sequences against miRBase mature miRNA sequence database using BLAST.[30] All the miRNAs quantified from each sample were then pulled together into an expression matrix for downstream analysis. Analysis of variance was used to identify miRNAs differentially expressed between conditions based on adjusted P value $< .05$ and at least 1 condition has median RPMs over 2. Raw fastq-files and processed data are available in GEO repository (GSE132801, GSE132795).

Extended Figure Legends:

Figure 1. miR-144 predicted target *Irg1* is downregulated in obese-induced insulin-resistant livers. (*A*) Selected significantly enriched GO biological processes of genes differentially expressed in LMs of 9- and 14-week-old *ob/ob* mice compared with WT mice (n = 4 WT, n = 3 *ob/ob* for 9 weeks; n = 4 for 14 weeks) based on RNA-seq data. The color and size of each node represents q-value ($-\log_{10}$) and gene number ratio ($N_{\_input\_genes}$ /$N_{\_background\_genes}$ in a GO term) from overrepresentation analysis (minimum and maximum node sizes stands for gene ratio 9.8% and 46.2%). The full list of significant biological processes is in Supplementary Tables 2 and 3. (*B*, *C*) Predicted cellular metabolism-associated (*B*) and related to glycolysis and TCA cycle (*C*) biological processes targeted by miR-144–5p in *ob/ob* mice. Colors in (*B*) represent their q-values ($-\log_{10}$) from false discovery rate multiple testing. Full list of overrepresented GO biological processes is in Supplementary Tables 4 and 5. (*D*) *Irg1* expression data from RNA-seq of 9- and 14-week-old WT and *ob/ob* mice (n = 4 WT, n = 3 for *ob/ob* at 9 weeks; n = 4 for *ob/ob* 14 weeks). (*E*, *F*) RT-qPCR analysis or western blots of *Irg1* in LMs (*E*) or whole livers (*F*) of mice fed an HFD or ND for 9 weeks (n = 3 per condition). (*G*, *H*) RT-qPCR analysis (*G*) and western blots (*H*) of *IRG1* in liver biopsies from lean, obese insulin-

sensitive (OIS) and obese insulin-resistant (OIR) human individuals (n = 3 per condition). Data are means ± SEM. *P < .05, **P < .01, ***P < .001.

Figure 4. *IRG1* silencing by miR-144 increases SDH and FH activities in the obese state. (*A*, *B*) RT-qPCR analysis of miR-144 (*A*) and *IRG1* (*B*) in human NPCs untreated, treated with FFAs and with scr, amiR-144 or after silencing *Irg1* (siIRG1, n = 3 per condition). Fold change (F.C.) to untreated treatment. (*C*, *D*) Measurement of SDH (*C*) and FH (*D*) activity in human NPCs untreated, treated with FFAs and with scr, amiR-144 or after silencing *Irg1* (siIRG1, n = 3 per condition). (*E*, *F*) Measurement of SDH (*E*) and FH (*F*) activity in human NPCs untreated, treated with LPS and with scr, mimic-miR-144 or after silencing *Irg1* (siIRG1, n = 3 per condition). (*G*) RT-qPCR analysis of *Irg1* in murine RAW264.7 cells untreated and treated with 10 or 100 ng of LPS (n = 2 technical replicate from 2 million pooled cells). Data are F.C. compared with untreated. (*H*) Measurement of itaconate intracellular levels in murine RAW264.7 cells untreated and treated with 10 or 100 ng of LPS (n = 2 technical replicate from 2 million pooled cells). (*I*, *J*) RT-qPCR analysis of miR-144 (*I*) and *Irg1* (*J*) in murine RAW264.7 cells untreated and treated with LPS or mimic-miR-144 (n = 2 technical replicate from 2 million pooled cells). (*K*) Measurement of itaconate intracellular levels in murine RAW264.7 cells untreated and treated with LPS, scr, or mimic-miR-144 (n = 2 technical replicate from 2 million pooled cells). (*L*) Binding model of itaconate within the catalytic site of FH as predicted by MD simulations. FH monomers are colored *yellow, cyan, and magenta*. Itaconate is shown as *blue sticks*; residues interacting with itaconate, or in close proximity to the molecule, are shown as *sticks* and are labeled. H-bond interactions are highlighted by *black dashed lines*. Nonpolar H atoms are omitted. (*M*) Representative structure (most populated cluster, with a population of 74% of MD frames) extracted from MD trajectories. FH monomers are colored *green, cyan, magenta, and yellow*. Itaconate is shown as *blue spheres*. Binding of itaconate to the FH catalytic site is highlighted by *black arrows*. (*N*) Main interactions established by itaconate within the FH catalytic site, by MD simulations. Data are means ± SEM and ± SD for (*G*–*K*). *P < .05, **P < .01, ***P < .001, and ****P < .0001.

References

1. Matthews DR, Hosker JP, Rudenski AS, et al. Homeostasis model assessment: insulin resistance and beta-cell function from fasting plasma glucose and insulin concentrations in man. Diabetologia 1985; 28:412–419.
2. Lee JH, Kim D, Kim HJ, et al. Hepatic steatosis index: a simple screening tool reflecting nonalcoholic fatty liver disease. Dig Liver Dis 2010;42:503–508.
3. Azzimato V, Jager J, Chen P, et al. Liver macrophages inhibit the endogenous antioxidant response in obesity-associated insulin resistance. Sci Transl Med 2020;12: eaaw9709.
4. Aouadi M, Tesz GJ, Nicoloro SM, et al. Orally delivered siRNA targeting macrophage Map4k4 suppresses systemic inflammation. Nature 2009;458:1180–1184.
5. Aparicio-Vergara M, Tencerova M, Morgantini C, et al. Isolation of Kupffer cells and hepatocytes from a single mouse liver. Methods Mol Biol 2017;1639:161–171.
6. Miller A, Nagy C, Knapp B, et al. Exploring metabolic configurations of single cells within complex tissue microenvironments. Cell Metab 2017;26:788–800.e6.
7. Gahan PB. C. J. F. Van Noorden and W. M. Fredericks. Enzyme histochemistry: A laboratory manual of current methods. Royal microscopical society handbooks No 26 Oxford Science Publication, Oxford, UK, 1992, £12.95, 116 pp. ISBN 019 856434 1 (Softback). Phytochemical Analysis 1993;4:240–241.
8. Fang B, Everett LJ, Jager J, et al. Circadian enhancers coordinate multiple phases of rhythmic gene transcription in vivo. Cell 2014;159:1140–1152.
9. Jacobson MP, Pincus DL, Rapp CS, et al. A hierarchical approach to all-atom protein loop prediction. Proteins 2004;55:351–367.
10. Ajalla Aleixo MA, Rangel VL, Rustiguel JK, et al. Structural, biochemical and biophysical characterization of recombinant human fumarate hydratase. FEBS J 2019;286:1925–1940.
11. Salomon-Ferrer R, Case DA, Walker DC. An overview of the Amber biomolecular simulation package. WIREs Comput Mol Sci 2013;3:198–210.
12. Anandakrishnan R, Aguilar B, Onufriev AV. H++ 3.0: automating pK prediction and the preparation of biomolecular structures for atomistic molecular modeling and simulations. Nucleic Acids Res 2012;40:W537–W541.
13. Humbert N, Kovalenko L, Saladini F, et al. Thia)calixarenephosphonic Acids as Potent Inhibitors of the Nucleic Acid Chaperone Activity of the HIV-1 Nucleocapsid Protein with a New Binding Mode and Multitarget Antiviral Activity. ACS Infect Dis 2020;6:687–702.
14. Dragoni F, Boccuto A, Picarazzi F, et al. Evaluation of sofosbuvir activity and resistance profile against West Nile virus in vitro. Antiviral Res 2020;175:104708.
15. Savoia M, Cencioni C, Mori M, et al. P300/CBP-associated factor regulates transcription and function of isocitrate dehydrogenase 2 during muscle differentiation. FASEB J 2019;33:4107–4123.
16. Spallotta F, Cencioni C, Atlante S, et al. Stable oxidative cytosine modifications accumulate in cardiac mesenchymal cells from type2 diabetes patients: rescue by alpha-ketoglutarate and TET-TDG functional reactivation. Circ Res 2018;122:31–46.
17. Roe DR, Cheatham TE 3rd. PTRAJ and CPPTRAJ: software for processing and analysis of molecular dynamics trajectory data. J Chem Theory Comput 2013; 9:3084–3095.
18. Miller BR, McGee TD, Swails JM, et al. MMPBSA.py: An Efficient Program for End-State Free Energy Calculations. J Chem Theory Comput 2012;8:3314–3321.
19. Bell CC, Hendriks DF, Moro SM, et al. Characterization of primary human hepatocyte spheroids as a model

system for drug-induced liver injury, liver function and disease. Sci Rep 2016;6:25187.
20. Dweep H, Gretz N. miRWalk2.0: a comprehensive atlas of microRNA-target interactions. Nat Methods 2015;12:697–697.
21. Morgantini C, Jager J, Li XD, et al. Liver macrophages regulate systemic metabolism through non-inflammatory factors. Nat Metab 2019;1:445–459.
22. Kim D, Pertea G, Trapnell C, et al. TopHat2: accurate alignment of transcriptomes in the presence of insertions, deletions and gene fusions. Genome Biol 2013;14:R36.
23. Liao Y, Smyth GK, Shi W. featureCounts: an efficient general purpose program for assigning sequence reads to genomic features. Bioinformatics 2014;30:923–930.
24. Quinlan AR, Hall IM. BEDTools: a flexible suite of utilities for comparing genomic features. Bioinformatics 2010;26:841–842.
25. Dobin A, Davis CA, Schlesinger F, et al. STAR: ultrafast universal RNA-seq aligner. Bioinformatics 2013;29:15–21.
26. Trapnell C, Williams BA, Pertea G, et al. Transcript assembly and quantification by RNA-Seq reveals unannotated transcripts and isoform switching during cell differentiation. Nat Biotechnol 2010;28:511–515.
27. Trapnell C, Hendrickson DG, Sauvageau M, et al. Differential analysis of gene regulation at transcript resolution with RNA-seq. Nat Biotechnol 2013;31:46–53.
28. Martin M. Cutadapt removes adapter sequences from high-throughput sequencing reads 2011;17:3.
29. Axtell MJ. ShortStack: comprehensive annotation and quantification of small RNA genes. RNA 2013;19:740–751.
30. Ye J, McGinnis S, Madden TL. BLAST: improvements for better sequence analysis. Nucleic Acids Res 2006;34:W6–W9.

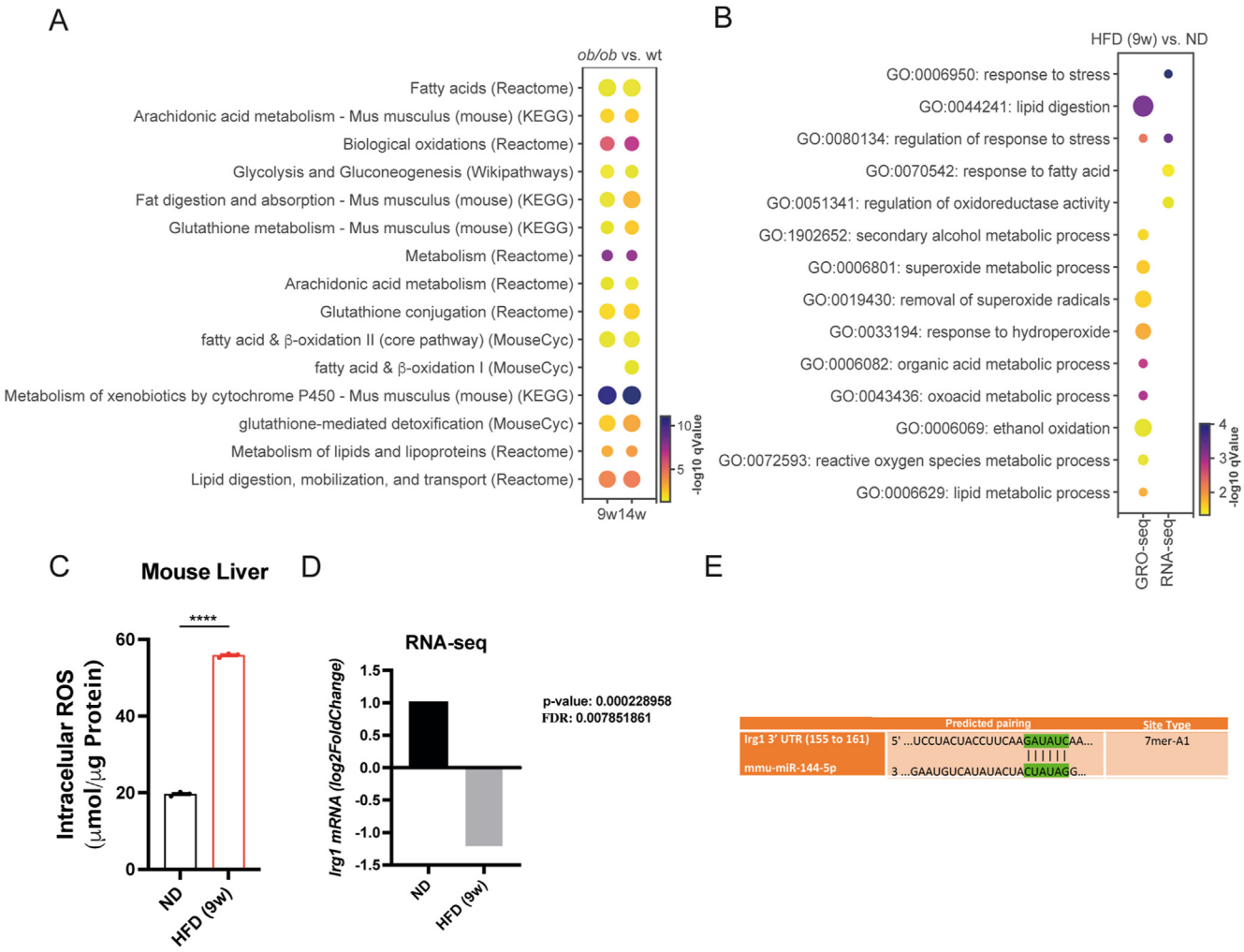

Supplementary Figure 1. (*A*) Selected significant overrepresented pathways enriched from genes differentially expressed in LMs of 9- and 14-week-old *ob/ob* mice compared with WT mice (n = 4 WT, n = 3 *ob/ob* for 9 weeks; n = 4 for 14 weeks) based on RNA-seq data. The color and size of each node represents q-value ($-\log_{10}$) and gene number ratio (N_{input_genes} /$N_{background\_genes}$ in a pathway term) from overrepresentation analysis (minimum and maximum node sizes stands for gene ratio 14.2% and 49.1%). Full list of significant pathways are in Supplementary Tables 6 and 7. (*B*) Selected significantly enriched GO biological process terms from genes differentially expressed in mice fed a HFD or ND for 9 weeks (n = 4 per condition) based on GRO-seq and RNA-seq data. The color and size of each node represents q-value ($-\log_{10}$) and gene number ratio (N_{input_genes}/$N_{background\_genes}$ in a GO term) from overrepresentation analysis (minimum and maximum node sizes stands for gene ratio 4.5% and 36.4%). Full list of significant biological processes are in Supplementary Tables 8 and 9. (*C*) Intracellular ROS levels of mice fed a HFD or ND for 9 weeks (n = 3 per condition) (*D*) *Irg1* expression data from RNA-seq of mice fed a HFD or ND for 9 weeks (n = 4 per condition). (*E*) Schematic representation of the predicted pairing between mmu-miR-144–5p seed sequence at 5′ untranslated (UTR) region and *Irg1* 3′ UTR region. Data are means ± SEM. ****$P < 0.0001$.

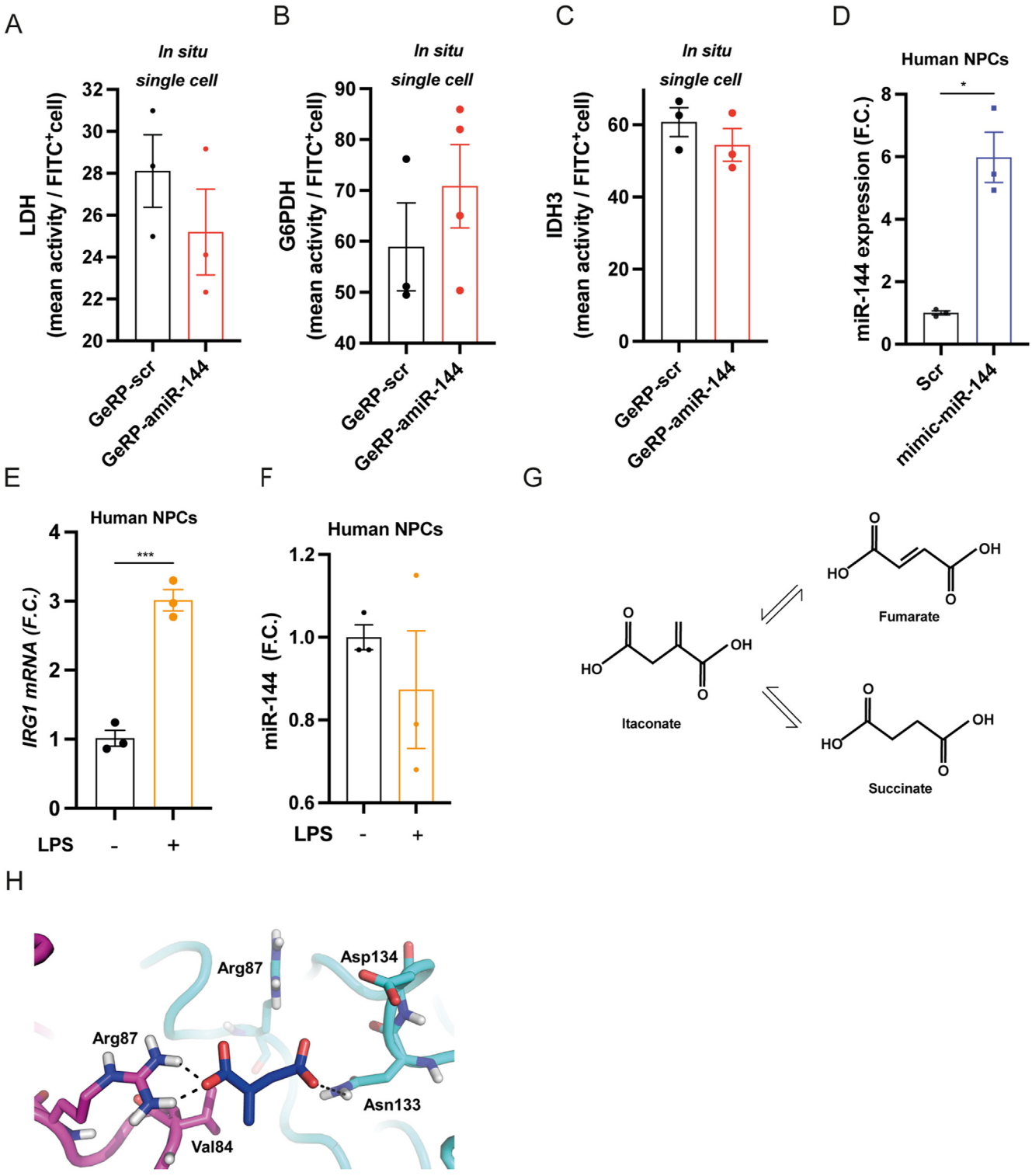

Supplementary Figure 2. (*A*–*C*) Measurements of LDH (*A*), G6PDH (*B*), and IDH3 (*C*) activities using single-cell enzyme histochemistry analysis in whole-mount liver sections from GeRP-scr and GeRP-amiR-144–treated mice (n = 3 per condition). (*D*) RT-qPCR analysis of miR-144 in human NPCs treated with scr or mimic-miR-144 (n = 3 per condition). Fold change (F.C.) calculation compared to scr. (E-F) RT-qPCR analysis of *IRG1* (*E*) and miR-144 (F) in human NPCs untreated or treated with LPS (n = 3 per condition) Fold change (F.C.) calculation compared with untreated treatment. (*G*) Molecular structures of itaconate, fumarate, and succinate. (*H*) Magnification of the interaction of itaconate within the additional site. Itaconate is shown as *blue sticks*; residues interacting with itaconate, or in close proximity to the molecule, are shown as *sticks* and are labeled. H-bond interactions are highlighted by *black dashed lines*. Nonpolar H atoms are omitted. Data are means ± SEM. $^{*}P < .05$, $^{***}P < .001$.

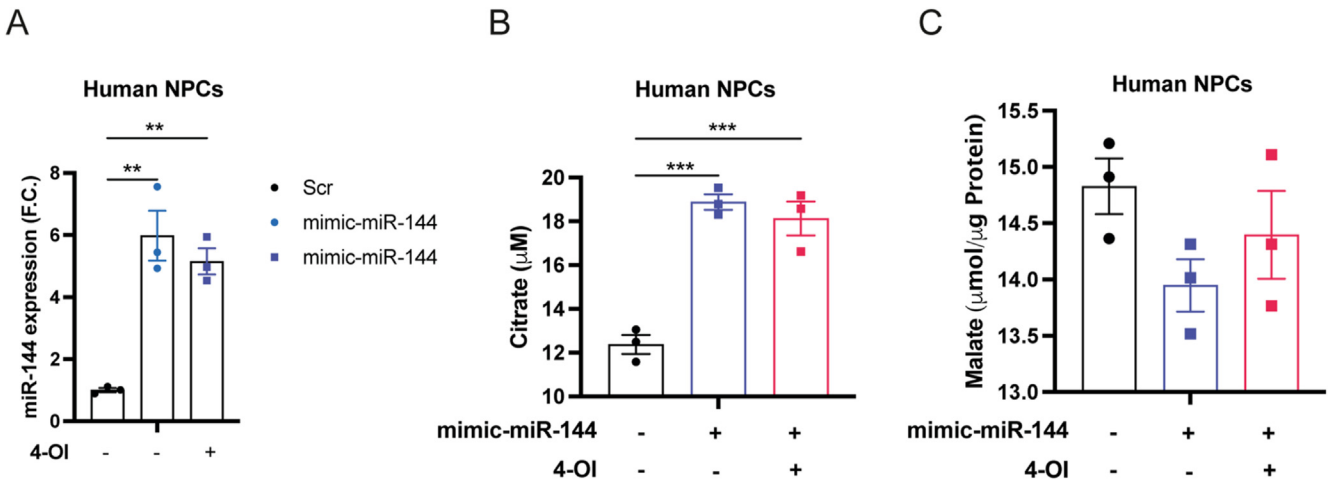

Supplementary Figure 3. (*A*) RT-qPCR analysis of miR-144 in human NPCs treated with scr, mimic-miR-144, and/or (n = 3 per condition). Fold change (F.C.) calculation compared with scr. (*B*, *C*) Measurement of intracellular citrate (*B*) and malate (*C*), amounts in human NPCs treated with scr, mimic-miR-144, and/or 4-OI (n = 3 per condition). Data are means ± SEM. **P* < .05, ***P* < .01, ****P* < .001, and *****P* < .0001.

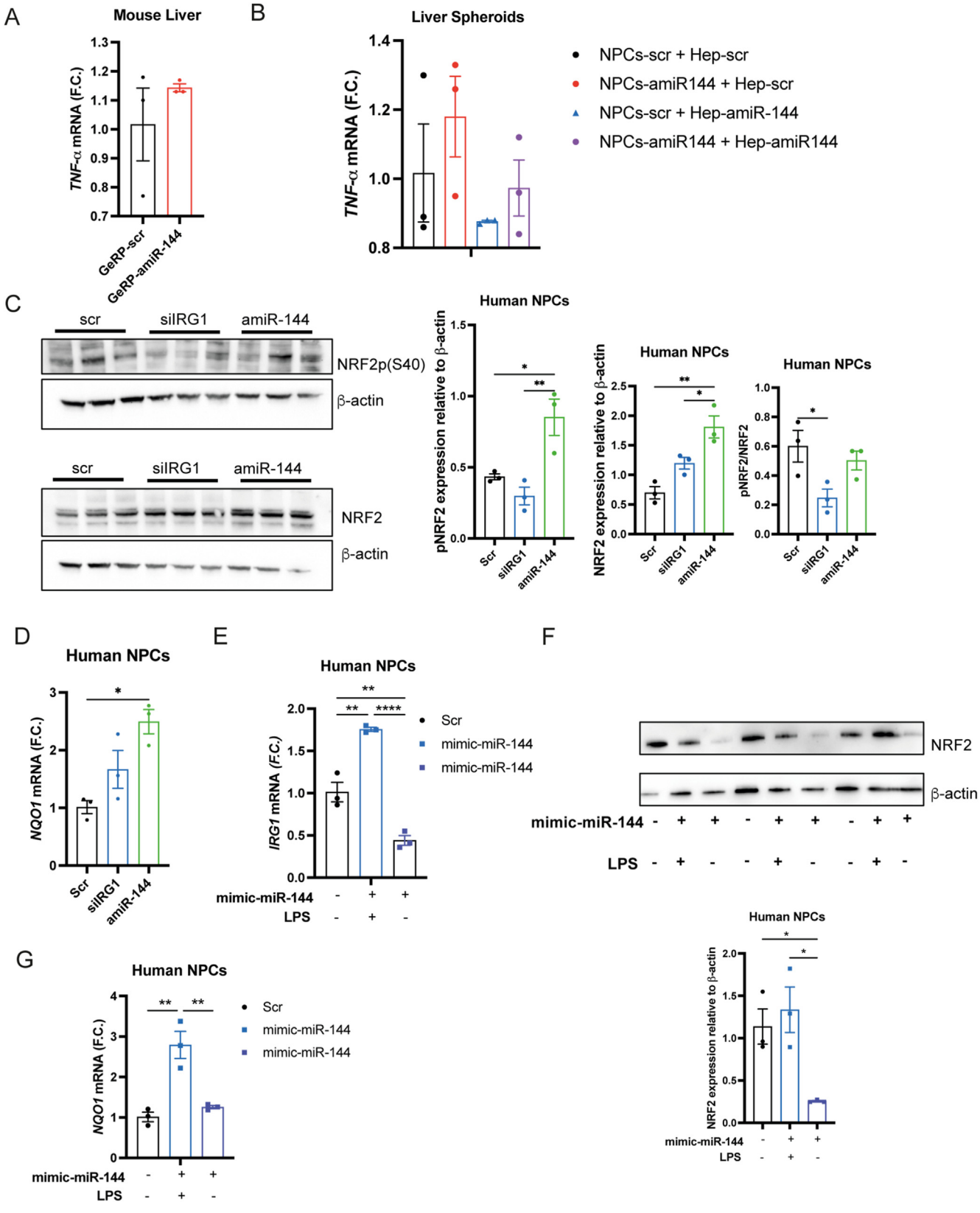
A
Mouse Liver
TNF-α mRNA (F.C.)
GeRP-scr
GeRP-amiR-144
B
Liver Spheroids
TNF-α mRNA (F.C.)
NPCs-scr + Hep-scr
NPCs-amiR144 + Hep-scr
NPCs-scr + Hep-amiR-144
NPCs-amiR144 + Hep-amiR144
C
scr
siIRG1
amiR-144
NRF2p(S40)
β-actin
NRF2
Human NPCs
pNRF2 expression relative to β-actin
NRF2 expression relative to β-actin
pNRF2/NRF2
D
Human NPCs
NQO1 mRNA (F.C.)
E
Human NPCs
IRG1 mRNA (F.C.)
mimic-miR-144
LPS
F
NRF2
β-actin
mimic-miR-144
LPS
G
Human NPCs
NQO1 mRNA (F.C.)
mimic-miR-144
LPS
Human NPCs
NRF2 expression relative to β-actin
mimic-miR-144
LPS

Supplementary Figure 4. (*A*) RT-qPCR analysis of *Tnf-α* whole livers from GeRP-scrambled control (scr)- and GeRP-amiR-144–treated mice (n = 3 per condition). Fold change (F.C.) calculation compared with GeRP-scr. (*B*) RT-qPCR analysis of *TNF-α* in human liver spheroids exposed to FFA and treated with amiR-144 or scr (pooled liver spheroids from 3 human donors). Data are F.C. compared with scr. (*C*) Western blot of NRF2 and NRF2 phosphorylation (pNRF2) on Serine40 in human NPCs treated with FFAs and with scr, amiR-144 or siIRG1 (n = 3 per condition). Quantification for pNRF2, NRF2, and pNRF/NRF2. (*D*) RT-qPCR analysis of *NQO1* in in human NPCs treated with FFAs and with scr, amiR-144, or siIRG1 (n = 3 per condition). (*E*) RT-qPCR analysis of *IRG1* in human NPCs treated with scr, LPS and/or mimic-miR-144 (n = 3 per condition). (*F*) Western blot and quantification of NRF2 in human NPCs treated with scr, LPS, and/or mimic-miR-144 (n = 3 per condition). (*G*) RT-qPCR analysis of *NQO1* in treated with scr, LPS, and/or mimic-miR-144 (n = 3 per condition). Data are F.C. compared with scr. Data are means ± SEM. $^{*}P < .05$, $^{**}P < .01$, $^{***}P < .001$, and $^{****}P < .0001$.